



## RESEARCH ARTICLE

10.1029/2018JB017207

# Fluid Injection Experiments in Shale at Elevated Confining Pressures: Determination of Flaw Sizes From Mechanical Experiments

Michael R. Chandler<sup>1</sup> , Julian Mecklenburgh<sup>1</sup> , Ernest Rutter<sup>1</sup> , and Peter Lee<sup>2,3</sup> <sup>1</sup>School of Earth and Environmental Sciences, The University of Manchester, UK, <sup>2</sup>Department of Mechanical Engineering, University College London, London, UK, <sup>3</sup>Research Complex at Harwell, Rutherford Appleton Laboratory, Didcot, UK**Key Points:**

- Smaller flaws control sample failure in shales than in most other rock materials
- Breakdown pressure increases linearly with confining pressure in fluid injection experiments
- Flaws in the region of 10- to 40- $\mu\text{m}$  length control sample failure

**Correspondence to:**M. Chandler,  
mike.chandler@manchester.ac.uk**Citation:**Chandler, M. R., Mecklenburgh, J., Rutter, E. H., & Lee, P. (2019). Fluid injection experiments in shale at elevated confining pressures: Determination of flaw sizes from mechanical experiments. *Journal of Geophysical Research: Solid Earth*, 124, 5500–5520. <https://doi.org/10.1029/2018JB017207>

Received 18 DEC 2018

Accepted 6 MAY 2019

Accepted article online 10 MAY 2019

Published online 21 JUN 2019

**Abstract** Triaxial experiments and direct fluid injection experiments have been conducted at confining pressures up to 100 MPa on Mancos shale, Whitby mudstone, Penrhyn slate, and Pennant sandstone. Experiments were conducted with sample axes lying both parallel and perpendicular to layering in the materials. During triaxial failure Penrhyn slate was stronger for samples with cleavage parallel to maximum principal stress, but the two orientations in the shales displayed similar failure stresses. Initial flaw sizes of around 40  $\mu\text{m}$  were calculated from the triaxial data using the wing crack model, with the shales having shorter initial flaws than the nonshales. During direct fluid injection, breakdown was rapid, with no discernible gap between fracture initiation and breakdown. Breakdown pressure increased linearly with confining pressure but was less sensitive to confining pressure than expected from existing models. A fracture mechanics-based model is proposed to determine the initial flaw size responsible for breakdown in injection experiments. Flaw sizes determined in this way agree reasonably with those determined from the triaxial data in the nonshales at low confining pressures. As confining pressure rises, a threshold is reached, above which the fluid injection experiments suggest a lower initial flaw length of around 10  $\mu\text{m}$ . This threshold is interpreted as being due to the partial closure of flaws. In the shales an initial flaw length of around 10  $\mu\text{m}$  was determined at all confining pressures, agreeing reasonably with those determined through the triaxial experiments.

## 1. Introduction

Mechanical properties of shales are of interest due to the worldwide exploitation of gas shale resources, as source or cap rocks in oil and gas exploration, and as a potential repository for radioactive waste. Hydraulic fracturing has become increasingly commonplace as a method of increasing hydrocarbon recovery from low-permeability reservoir rocks such as shale and tight sandstones, leading to increased interest in fracture growth properties in these materials (Rutter & Hackston, 2017). This increased interest has led to a number of recent studies investigating fracture mechanics properties in shale materials both through experimental measurements (Chandler et al., 2016, 2018; Forbes Inskip et al., 2018; Lee et al., 2015; Luo et al., 2018) and modeling studies (Dutler et al., 2018; Gao et al., 2018; Zia et al., 2018).

### 1.1. Fracture Mechanics in Rock Mechanics

The field of fracture mechanics seeks to understand failure of materials in the presence of initial flaws and is concerned with finding the relationship between the material, the stresses applied, and the size of the flaw that leads to failure (Janssen et al., 2002). The material's resistance to fracture is represented through the critical stress intensity factor of a mode-I fracture, known as the fracture toughness,  $K_{Ic}$ . Equation (1) defines the failure stress according to Linear Elastic Fracture Mechanics through the Griffith criterion. The failure stress,  $\sigma_f$ , is given as a function of the fracture toughness,  $K_{Ic}$ , the initial flaw size,  $a$ , and a geometric factor,  $\iota$ , accounting for the geometry of the flaw within the material (Paterson & Wong, 2005). Tada et al. (2000) summarize the calculation of  $\iota$  for a wide range of geometries. The greater the size,  $a$ , of the initial flaw, the lower the failure stress.

$$\sigma_f = \frac{K_{Ic}}{\iota\sqrt{\pi a}} \quad (1)$$

©2019. The Authors.

This is an open access article under the terms of the Creative Commons Attribution License, which permits use, distribution and reproduction in any medium, provided the original work is properly cited.

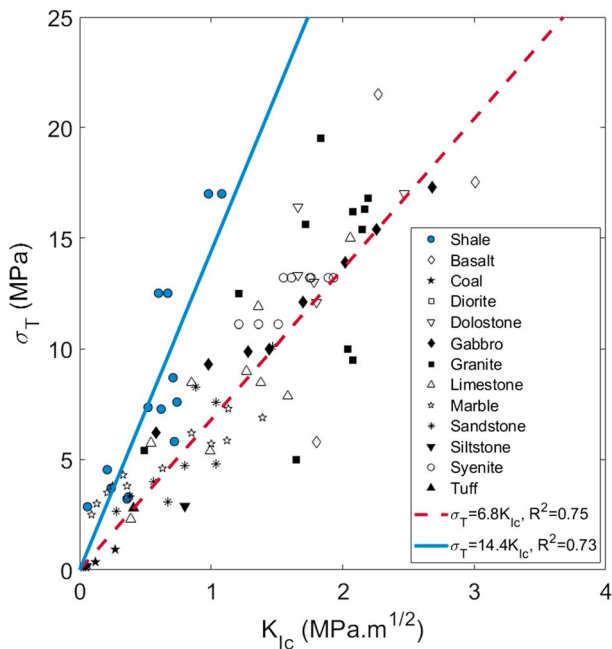


**Figure 1.** Tensile strength,  $\sigma_T$ , as a function of mode-I fracture toughness,  $K_{Ic}$ , for a range of rock materials. The nonshale materials are from Zhang (2002) and Chandler et al. (2016), while the shale materials are from Schmidt and Huddle (1977), Chandler et al. (2016), Forbes Inskip et al. (2018), and Chandler et al. (2018). The dashed and solid lines are least squares fits made to the nonshale and shale data sets, respectively (and forced to intercept the origin).

While the recent studies referenced above provide a great deal of insight into  $K_{Ic}$  in low-permeability materials, determining the required failure stresses also requires knowledge of the size of the initial flaws. During fracture toughness experiments, this requirement is sidestepped by manufacturing a large artificial flaw (a notch) into the material prior to the experiment.  $l$  and  $a$  are therefore known prior to the experiment, and  $\sigma_f$  is determined while loading. These values can then be used with equation (1) to determine  $K_{Ic}$  for the material.

In principle, the same relationship can be used in a material of known  $K_{Ic}$  (measured through previous experiments), to determine the initial flaw size,  $a$ , from  $\sigma_f$  if a realistic geometry (i.e.,  $l$ ) can be assumed. Here, triaxial experiments and direct fluid injection experiments were performed on two shales: the Mancos shale and Whitby mudstone, a tight-gas sandstone analogue; Pennant sandstone, and a slate with anisotropy derived from cleavage planes; Penrhyn slate. For each of these materials, fracture toughness measurements exist in the scientific literature (Chandler et al., 2018), and it is therefore possible to analyze the results in terms of the characteristic flaw size controlling the sample failure, in addition to the more standard experimental data processing associated with each type of experiment.

Zhang (2002) suggest that fracture toughness and tensile strength should be related under quasi-static loading because the tensile fracture occurs due to the extension of a single crack in each case, and similar fracture surfaces are seen in each type of experiment. Figure 1 shows the tensile strength,  $\sigma_T$ , of a wide range of rock types all plotted as a function of their mode-I fracture toughness,  $K_{Ic}$ . These data were compiled from Zhang (2002), Schmidt and Huddle (1977), Chandler et al. (2016), Forbes Inskip et al. (2018), and Chandler et al. (2018). The relationship between  $\sigma_T$  and

$K_{Ic}$  should be independent of the method used to determine each parameter, provided the samples were of sufficient size in each case. The various shale rocks are plotted in solid blue circles, while all other rocks are plotted in black and white. The shales demonstrate a slightly stronger dependence of  $\sigma_T$  on  $K_{Ic}$  than the other rock types in general, by sitting slightly above the main trend.

By rearranging equation (1) to show  $\sigma_T/K_{Ic}$ , it is apparent that the steeper dependence of  $\sigma_T$  on  $K_{Ic}$  in the shale suggests that mode-I fracture initiation in shale may be controlled by a smaller flaw size than that in other rock types in general. These initial flaws are important controllers of bulk failure within rocks, because the initiation of ruptures over a wide range of length scales will be caused by stress concentrations on these small initial flaws. Hence, the mechanical data are used here in order to attempt to derive flaw sizes controlling the observed mechanical behavior, and whether these differ between shales and other rock materials.

### 1.2. Laboratory-Scale Fluid Injection Experiments

Laboratory-scale fluid injection experiments on rock materials are quite rare in the literature. Experiments fall into two distinct types, being direct fluid injection and sleeve fracturing. Direct fluid injection experiments similar to those conducted here involve the injection of pressurized fluid directly into a borehole, with the injected fluid having access to the progressing fracture. The fluid pressure rises until a fracture initiates from the borehole wall. Once the fracture reaches the edge of the sample, the injected fluid leaks out and the injection pressure drops rapidly.

Lockner and Byerlee (1977), Zoback et al. (1977), Song et al. (2001), and Stanchits et al. (2015) all conducted direct fluid injection of low-viscosity fluids into sandstones under pressurization rate control. Each of these studies found a linear increase in breakdown pressure with confining pressure, and rapid, uncontrolled breakdown once the peak injection pressure was reached. Zoback et al. (1977), Bungler and Detournay (2008), Stanchits et al. (2015), and Lecampion et al. (2017) found that for experiments injecting higher-viscosity fluids, the breakdown pressure can be higher than the fracture initiation pressure, in agreement with the models summarized by Detournay (2016).

Most studies into laboratory-scale fluid injection experiments find borehole failure through one or two radial fractures from the borehole wall. Lockner and Byerlee (1977) observed a shift from failure in shear at low injection rates toward opening mode failure with faster injection. In anisotropic shales, failure geometries can be more complex. Li et al. (2016) observe fail along the bedding planes and normal to the borehole direction in their Green River oil shale samples, while Rutter and Mecklenburgh (2017) observed short opening mode fractures connected by bedding-parallel shear mode segments in 60-mm-diameter samples of Whitby mudstone. Warpinski et al. (1987) performed fluid injection experiments into cuboid samples featuring machined joints and found a complex dependency of the fracture propagation on parameters relating to the joints, including joint orientation, spacing, and frictional properties.

Sleeve fracturing experiments involve the pressurization of a polymer tube within the borehole. These experiments behave similarly to direct fluid injection experiments except that the injection fluid does not have access to the developing fracture, effectively simulating the fast pressurization state described by Ito and Hayashi (1991) and Detournay and Carbonell (1997). These experiments remove the complex poroelastic effects potentially caused by the injection fluid seeping into the pores of the rock sample (Abou-Sayed et al., 1978; Clifton et al., 1976; Schmitt & Zoback, 1992).

Sleeve fracturing experiments have been performed by Vinciguerra et al. (2004) and Stoeckhert et al. (2014, 2015) on samples of Darley Dale sandstone, Berbetal sandstone, and anisotropic Fredeburg slate, respectively. In each study, gradual fracture propagation was observed, with fracture length increasing as a function of  $P_{inj}$ . Stoeckhert et al. (2015) found that in the slate under uniaxial compression, fracture orientation was controlled by cleavage planes at low applied pressure (strength-dominated fracture orientation) but found a transition to a stress-dominated fracture orientation at around 5- to 10-MPa applied stress.

Ishida et al. (2004) compared sleeve fracturing and direct fluid injection experiments into 190-mm cubic samples of Kurokamijima granite at constant injection rate under low confining pressures. Using the sleeve fracturing technique, they were able to propagate fractures gradually but found unstable fracture propagation during their direct fluid injection experiments, independent of injection fluid viscosity.

### 1.2.1. Theoretical Models for the Variation of Breakdown Pressure on Confining Pressure During Fluid Injection Experiments

A variety of models exist for the dependence of the breakdown pressure on the far-field stresses during fluid injection experiments, which are described briefly here. Breakdown criteria in the literature fall into three main groups: those based on the circumferential stress on the wellbore surface (Haimson & Fairhurst, 1967; Hubbert & Willis, 1972), those based on the circumferential stress over a characteristic length scale (Detournay & Cheng, 1992; Ito & Hayashi, 1991; Song et al., 2001), and those based on fracture mechanics (Abou-Sayed et al., 1978; Detournay & Carbonell, 1997; Zhang et al., 2017). Throughout this section, a vertical borehole is assumed in a body where  $\sigma_v > \sigma_{H,max} > \sigma_{H,min}$ , so that  $\sigma_1$  is acting parallel to the wellbore axis, and  $\sigma_2, \sigma_3$  are acting in the plane normal to the borehole direction.

Both the Hubbert and Willis (1972) and Haimson and Fairhurst (1967) breakdown criteria are based on the assumption that the failure occurs when the circumferential Terzaghi effective stress at the borehole wall reaches the tensile strength of the sample. Hubbert and Willis (1972) derived the solution for the breakdown pressure of a circular borehole in a case where there is no fluid penetration into the borehole wall:

$$P_{breakdown} = 3\sigma_3 - \sigma_2 + \sigma_T - P_{pore} \quad (2)$$

where  $\sigma_3$  and  $\sigma_2$  are the minimum and maximum horizontal far-field stresses,  $\sigma_T$  is the tensile strength of the material, and  $P_{pore}$  is the far-field pore pressure. Haimson and Fairhurst (1967) derived an expression that is valid for permeable rocks by assuming that the rock near to the wellbore behaves poroelastically:

$$P_{breakdown} = \frac{3\sigma_3 - \sigma_2 + \sigma_T - 2 \left[ \frac{\alpha(1-2\nu)}{2(1-\nu)} \right] P_{pore}}{2 \left( 1 - \left[ \frac{\alpha(1-2\nu)}{2(1-\nu)} \right] \right)} \quad (3)$$

where  $\nu$  is Poisson's ratio and  $\alpha$  is the Biot effective stress parameter, which defines the relative effects of confining and pore pressure on effective stress through

$$\sigma^{eff} = P_{conf} - \alpha P_{pore} \quad (4)$$

However, various authors have noted the difficulties in resolving the Hubbert and Willis (1972) and Haimson and Fairhurst (1967) criteria, in that there is no discrete cutoff between permeable and impermeable in rock materials. There is also a disagreement between equations (2) and (3) in that for the limit of an impermeable system ( $\alpha = 0$  in equation (3)), the Hubbert and Willis (1972) model predicts the breakdown pressure to depend twice as strongly on the confining pressure as the Haimson and Fairhurst (1967) model.

Neither the Hubbert & Willis criterion nor the Haimson & Fairhurst criterion features any dependence on the pressurization rate, despite this having a strong effect on breakdown pressure in some studies (Haimson & Zhao, 1991; Ito & Hayashi, 1991; Schmitt & Zoback, 1992).

Ito and Hayashi (1991), Detournay and Cheng (1992), and Song et al. (2001) argue that because the pores around a borehole in a permeable rock are connected, it is difficult to envisage exactly what an initial flow corresponds to. They develop criteria in which fracture occurs at the borehole surface when the effective stress reaches the tensile strength at a point that is some distance,  $d$ , into the rock from the borehole surface. Distance  $d$  is a material constant known as the characteristic length of tensile failure.

Ito and Hayashi (1991) derive functions for the breakdown pressure in two limiting cases of borehole pressurization rate,  $A$ . The fast pressurization case ( $A \rightarrow \infty$ ) is analogous to an impermeable material and the fluid pressure in the cracks remains at its initial value while the borehole pressure rises. The slow pressurization case ( $A \rightarrow 0$ ) is analogous to a highly permeable material, and the fluid pressure in the cracks remains at its initial value while the borehole pressure rises.

$$P_{\text{breakdown}} = \begin{cases} \left(1 + \frac{d}{r_{\text{bore}}}\right)^2 (\sigma_T - S_\theta - P_{\text{pore}}) + P_{\text{pore}}, & (A \rightarrow \infty) \\ \frac{2(\sigma_T - S_\theta - P_{\text{pore}})}{\left(1 + \frac{1}{\left(\frac{d}{r_{\text{bore}}}\right)^2}\right)^2} + P_{\text{pore}}, & (A \rightarrow 0) \end{cases} \quad (5)$$

where

$$S_\theta = \frac{\sigma_1 + \sigma_3}{2} \left(1 + \frac{r_{\text{bore}}^2}{(d + r_{\text{bore}})^2}\right) - \frac{\sigma_1 - \sigma_3}{2} \left(1 + \frac{3r_{\text{bore}}^4}{(d + r_{\text{bore}})^4}\right) + \frac{r_{\text{bore}}^2}{(d + r_{\text{bore}})^2} P_{\text{pore}} \quad (6)$$

and

$$d = \frac{1}{2\pi} \left(\frac{K_{\text{Ic}}}{\sigma_T}\right)^2 \quad (7)$$

$r_{\text{bore}}$  is the radius of the borehole. When  $d/r_{\text{bore}}$  becomes very large, the two conditions in equation (5) reduce to equations (2) and (3), respectively (Zhang et al., 2017). Song et al. (2001) expand this type of model by allowing the material to have different sensitivities to pore and confining pressures.

Abou-Sayed et al. (1978), Detournay and Carbonell (1997), and Zhang et al. (2017) use fracture mechanics to consider a borehole with two symmetric small radial flaws. Detournay and Carbonell (1997) consider the borehole walls to be impermeable and the same two limiting pressurization rates proposed by Ito and Hayashi (1991). They are able to show that for slow pressurization, crack propagation will always be unstable but that fracture propagation can be stable under fast pressurization. However, for cracks of any meaningful size this limiting case is impossible to reach unless the borehole is jacketed as in a sleeve fracturing experiment. They are also able to show that their solution is equivalent to the Hubbert and Willis (1972) and Haimson and Fairhurst (1967) criteria in the case of fast and slow pressurization, respectively. Zhang et al. (2017) expand these models by considering permeation effects at the borehole walls.

## 2. Materials and Methods

Triaxial deformation experiments and fluid injection experiments were conducted on four rock types. For the shales, cores were taken parallel and perpendicular to bedding, while in the slate cores were taken parallel and perpendicular to the cleavage planes. Pennant sandstone samples were taken perpendicular to bedding.  $K_{\text{Ic}}$  values for these materials were determined by Chandler et al. (2018) and are listed in Table 1.

**Table 1**  
Properties of the Materials Tested Here

| Parameter         | Units               | Whitby mudstone                          |                       | Mancos shale                        |                       | Penrhyn slate          |                        | Pennant sandstone          |
|-------------------|---------------------|--|-----------------------|-------------------------------------|-----------------------|------------------------|------------------------|----------------------------|
|                   |                     | Bedding parallel                         | Bedding perpendicular | Bedding parallel                    | Bedding perpendicular | Cleavage parallel      | Cleavage perpendicular | Bedding perpendicular      |
| $K_{IC}$          | $MPa \cdot m^{1/2}$ | 0.06                                     | $0.37 \pm 0.23$       | $0.31 \pm 0.01$                     | $0.44 \pm 0.07$       | $0.94 \pm 0.13$        | $0.88 \pm 0.08$        | $0.32 \pm 0.06$            |
| $\sigma_T$        | MPa                 | $2.86 \pm 1.14$                          | $3.21 \pm 0.64$       | $4.54 \pm 0.16$                     | $5.81 \pm 0.57$       | —                      | —                      | 15.1                       |
| Reference         |                     | Chandler et al. (2018)                   |                       | Chandler et al. (2016)              |                       | -                      |                        | Chandler et al. (2018)     |
| $\bar{d}_{grain}$ | mm                  | 0.010–0.050 (silt)<br>0.001–0.010 (clay) |                       | 0.002–0.063 (silt)<br><0.002 (clay) |                       | 0.030–0.075            |                        | 0.2000 (quartz)            |
| Reference         |                     | McKernan et al. (2017)                   |                       | Leckie et al. (1991)                |                       | Cárdenes et al. (2014) |                        | Hackston and Rutter (2016) |
| $\epsilon_{dry}$  |                     | 11%                                      |                       | 24%                                 |                       | 20%                    |                        | 7.5%                       |
| $\phi_{open}$     |                     | 6–9%                                     |                       | 4%                                  |                       | 1%                     |                        | $4.57 \pm 0.23\%$          |
| Reference         |                     | McKernan et al. (2017)                   |                       | Chandler et al. (2016)              |                       | This study             |                        | Hackston and Rutter (2016) |

Note.  $K_{IC}$  values are reproduced from Chandler et al. (2018) except for the Penrhyn slate. For the Penrhyn slate,  $K_{IC}$  was determined using the same method. Mean grain diameters,  $\bar{d}_{grain}$ ,  $P$  wave anisotropies,  $\epsilon_{dry}$ , and open porosities,  $\phi_{open}$ , are also listed alongside the references from which they are reproduced.

## 2.1. Rock Types Tested

Triaxial experiments were conducted on Whitby mudstone, Mancos shale, Pennant sandstone, and Penrhyn slate.

*Whitby mudstone* was deposited within the Cleveland basin, (NE England) during the Jurassic period and is a silty mudstone, which is often used as an analogue for Posidonia shale. The material used here was collected from the intertidal zone at Runswick Bay, Yorkshire, UK, and is described in some detail by McKernan et al. (2014, 2017) who used helium porosimetry to measure porosities between 6% and 9%. Ultrasonic  $P$  wave velocity anisotropy was measured at ambient conditions on dry samples with a diameter of 50.8 mm. In the bedding-parallel orientation,  $v_p$  was found to be  $3.47 \pm 0.04$  km/s, with a lower velocity of  $3.06 \pm 0.05$  km/s found in the bedding-perpendicular direction. Following the method described by Berryman (2008, their equation 32), these velocities imply a  $P$  wave anisotropy of  $\epsilon_{dry} = 11\%$ .

*Mancos shale* is an Upper Cretaceous shale deposited 90–70 Ma in the Rocky Mountain area of western Colorado and eastern Utah (USA) and provides the source for many of the shale plays in the Rockies (Longman & Koepsell, 2005). The material used here is made up of thinly laminated interbedded silt and claystones and is described in detail by Chandler et al. (2016), who found an open helium porosity of  $\phi_{open} = 4\%$ , a total helium porosity of  $\phi_{total} = 9\%$ , and a dry  $P$  wave anisotropy of  $\epsilon_{dry} = 24\%$ .

*Pennant sandstone* is an Upper Carboniferous quartz sandstone from South Wales (UK), described in detail by Hackston and Rutter (2016). Pennant sandstone is near mechanically isotropic and is made up of 70% quartz grains and 15% feldspar, with the interstices filled with muscovite, oxides, and clay minerals. Hackston and Rutter (2016) measured an open porosity of  $\phi_{open} = 4.57 \pm 0.23\%$  using gravimetry and helium pycnometry, and measured an ultrasonic  $P$  wave anisotropy of  $\epsilon_{dry} = 7.5\%$ .

*Penrhyn slate* is a metamorphosed Lower Cambrian mudstone from North Wales (UK; McCrae et al., 1979). The slate features cleavage planes at a high angle to the original bedding planes. The orientation of these cleavage planes can be identified by the ellipsoidal reduction spots visible in the material. X-ray diffraction measurements were conducted on these samples and found the rock to be made up of 49% quartz, 13% clinocllore, 10% albite, 10% muscovite, 7% hematite, and 11% epidote.  $\phi_{open}$  was found to be  $\approx 1\%$  using Helium porosimetry. Ultrasonic  $P$  wave anisotropy was found to be  $\epsilon_{dry} = 20\%$  following the method of Berryman (2008).

## 2.2. Sample Dimensions and Manufacture

Cylindrical rock samples cut to nominal dimensions of  $25.4 \pm 0.4$ -mm diameter and  $50.8 \pm 3.0$ -mm length were fabricated by coring from blocks of the sample materials. The sample ends were ground flat and parallel to an accuracy of 0.01 mm using a lapping wheel. Shale samples were dried at ambient conditions until their

mass stabilized to within 0.01-g variation over 24 hr. This took approximately 3 weeks, but these shales have previously been found to delaminate when dried at 60°. Pennant sandstone and Penrhyn slate samples were dried to the same accuracy, but within an oven kept at 60 °C. All experiments were conducted on dry samples. Chen et al. (2019) found the presence of water to reduce  $K_{Ic}$  by approximately 50% in clay-rich shales. For the analyses presented here, the saturation state of the samples is the same as that used by Chandler et al. (2018), from which  $K_{Ic}$  was determined. Therefore, the  $K_{Ic}$  values used should correspond to the same saturation state as the experiments conducted here.

Chandler et al. (2018) found the yielding zone around progressing fractures in these materials to be around  $r_y \sim 40 \mu\text{m}$ , and the critical radii as defined by Schmidt and Huddle (1977) to be around  $r_c \sim 250 \mu\text{m}$ . These correspond to  $r_{\text{sample}}/r_y \sim 600$  and  $r_{\text{sample}}/r_c \sim 50$ , respectively. Therefore, the zone of inelastic deformation around the fracture tip is expected to be small relative to the sample size, and consequently, these sample sizes are expected to be large enough to maintain the small-scale yielding criterion.

These cylindrical samples were used for both the triaxial experiments and the fluid injection experiments. A blind-ending borehole with a diameter of 1.2 mm was drilled  $25.4 \pm 1$  mm into each fluid injection sample, along the cylinder axis. In Whitby mudstone and Penrhyn slate, experiments were not conducted in the bedding-/cleavage-parallel orientation. While drilling the central borehole, these materials were prone to axial splitting along the bedding/cleavage planes, and sample manufacture was not successful.

Haimson and Zhao (1991) investigated the effect of borehole size on breakdown pressure in samples of Lac du Bonnet granite and Indiana limestone. They found a large sensitivity to borehole diameter for diameters less than 13 mm, but it should be noted that the materials tested by Haimson and Zhao (1991) feature grain diameters 2–4 orders of magnitude larger than those tested here. Cuss et al. (2003) and Meier et al. (2013) investigate size effects relating to borehole failure under increasing confining pressure with zero borehole pressure. Cuss et al. studied samples of sandstones, while Meier et al. conducted their experiments on samples of Posidonia shale. Both studies found a nonlinear increase in breakout pressure with reducing borehole diameter. Each study found that as borehole diameter falls toward a point where the borehole wall curvature is comparable to grain size, breakout pressure becomes increasingly sensitive to borehole diameter. Cuss et al. (2003) demonstrated that for breakdown driven by grain-crushing, a range of rocks lay on a single trend when breakdown pressure was normalized according to  $d_{\text{bore}}/(\phi d_{\text{grain}})$ , with breakdown pressure becoming increasingly insensitive to  $d_{\text{bore}}$  once  $d_{\text{bore}}/(\phi d_{\text{grain}})$  rose above  $\approx 400$ . In the experiments conducted here,  $d_{\text{bore}}/(\phi d_{\text{grain}})$  is in the region of  $\approx 900$  for Pennant sandstone, up to  $\approx 20,000$  for the shales. Therefore, while the mechanics of the borehole failure do vary between the borehole breakout experiments of Cuss et al. (2003), Meier et al. (2013) and those conducted here, the experiments conducted here are believed to be within a regime where the sensitivity of breakdown pressure to borehole diameter is low.

### 2.3. Triaxial Experimental Method

Standard triaxial experiments were conducted using the “Phoenix” triaxial deformation apparatus at the University of Manchester rock deformation laboratory. The samples were jacketed to isolate them from the Di-ethylhexyl sebacate confining fluid (Rheolube DOS<sup>®</sup>) using heat-shrink polymer tubing, which does not contribute any load-bearing capacity to the sample assembly ( $\leq 0.1$  MPa). The desired confining pressure was applied using an air-driven pump. The samples were not stress cycled to a higher confining pressure prior to the experiments, and no friction reducing material was used on the interface between sample and steel loading pistons.

Axial stress was applied via a balanced piston driven by an actuator system at the bottom of the pressure vessel assembly to provide a constant strain rate of  $\dot{\epsilon} = 2 \times 10^{-5} \text{ s}^{-1}$  at constant confining pressure, and the sample was loaded until failure. Axial stress and strain were recorded using a Heard-type internal force gauge and an externally mounted potentiometric displacement transducer respectively. Confining pressure was servo controlled. A steel sample was used to measure a machine stiffness of  $0.036 \pm 0.008 \text{ mm/kN}$ , allowing the determination of axial machine distortion and hence the true axial specimen displacement.

The triaxial data were processed to obtain the failure criterion as the tangent to a family of Mohr circles, following the steps laid out by Zhao (2000). The  $\sigma_1$  at failure is plotted as a function of  $\sigma_3$  for each rock type in Figure 4. The intercept of this plot corresponds  $\sigma_c$ , the uniaxial compressive strength. The  $\tan(\zeta)$  is the slope of the strength envelope in principal stress space (i.e., the gradient of  $\sigma_{1,\text{fail}}(\sigma_3)$ ). The friction angle,  $\phi$ ,

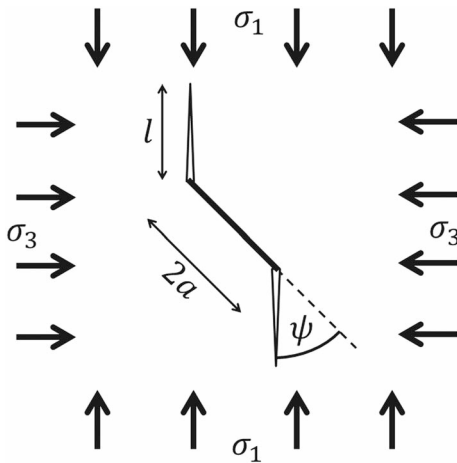


**Figure 2.** The wing crack model of Ashby and Sammis (1990). A small flaw of length  $2a$  oriented at an angle  $\psi$  to the largest principal stress,  $\sigma_1$  begins to slide, causing a mode-I stress intensity factor,  $K_I$  at either end of the flaw. At the point that this stress intensity reaches the fracture toughness, ( $K_I = K_{Ic}$ ), wing cracks initiate from the flaw in a direction parallel to  $\sigma_1$ . Figure modified after Ashby and Sammis (1990).

was then calculated through

$$\varphi = \arcsin \left( \frac{\tan \zeta - 1}{\tan \zeta + 1} \right). \quad (8)$$

The sliding friction coefficient was calculated through

$$\mu_s = \tan \varphi. \quad (9)$$

The cohesion,  $C$  was calculated by

$$C = \frac{\sigma_c}{2(\tan \zeta)^{\frac{1}{2}}} \quad (10)$$

following Zhao (2000).

#### 2.4. Flaw Size Determination Using the Wing Crack Model of Triaxial Failure

Following Bonnelye et al. (2017), the triaxial data presented here were processed using a method based on the wing crack model of Ashby and Sammis (1990), as shown in Figure 2. The wing crack model explains failure of a rock sample under compressive stresses as being due to sliding on shear-oriented small flaws that could be cracks or grain boundary segments, causing the opening of mode-I “wing” cracks at the flaw tips.

These cracks and flaws are eventually able to interconnect, leading to failure of the material.

The wing crack model can be expressed as

$$\sigma_1 = \left[ \frac{(1 + \mu_i^2)^{1/2} + \mu_i}{(1 + \mu_i^2)^{1/2} - \mu_i} \right] \sigma_3 - \left[ \frac{\sqrt{3}}{(1 + \mu_i^2)^{1/2} - \mu_i} \right] \frac{K_{Ic}}{\sqrt{\pi a}}, \quad (11)$$

where  $\sigma_1$  and  $\sigma_3$  are the principal stresses at the point at which the propagation of wing cracks begins.  $K_{Ic}$  is the fracture toughness of the material, the critical value of the stress intensity beyond which a fracture will propagate rapidly. The internal friction coefficient,  $\mu_i$  accounts for small-scale grain on grain sliding, and  $a$  is the half-length of the small flaw from which the wing cracks nucleate (Bonnelye et al., 2017). Equation (11) was derived by Ashby and Hallam (1986) for an angle,  $\psi$  (as defined in Figure 2), at which the stress intensity is maximized. Essentially then, a population of flaws with a random distribution of angles is assumed, and failure is assumed to be controlled by the most preferentially aligned flaws. In shales and slates, the population of flaw angles within the sample material is unlikely to have a random distribution of angles, but here we follow Bonnelye et al. (2017) in assuming that sufficient flaws do exist at this angle to initiate the bulk failure.

The stress required for the initialization of growth is lower than the stress at which bulk failure actually occurs in compression, even if a proportionality might be expected between them. Here, the axial stress at the onset of nonlinearity,  $\sigma_{1, \text{nonlinearity}}$ , is taken to correspond to this initial growth of wing cracks. Essentially, the initiation of these wing cracks is assumed to cause the deviation of the axial stress-strain curve from linear. This is likely to overestimate slightly the stress at which the wing cracks begin to open, as axially opening flaws would be observed in the circumferential strain prior to the axial strain. The circumferential strain was not measured during these experiments, so the value found from the axial strain was used instead and should be thought of as a maximum value for the stress at the onset of opening.

Using equation (11), it can be seen that a plot of  $\sigma_1$  at the onset of nonlinearity as a function of  $\sigma_3$  should be linear with a gradient dependent solely on  $\mu_i$  (through the function in the first set of square brackets). The intercept of the same plot is then dependent on  $\mu_i$ ,  $K_{Ic}$ , and  $a$  through the function in the second set of square brackets. Hence, for a material of known fracture toughness, the internal friction coefficient and initial flaw size can be determined from a series of triaxial experiments conducted at different confining pressures.

It should be noted that while the wing crack model is applied here in a preliminary analysis, it is not necessarily universally applicable, as opening mode cracks can form without any sliding on a shearing interface.

Mode-I cracks can also form as the result of an indentation effect or elastic contrasts between grains for example. Using machined flaws in Gypsum, Bobet (2000) also identifies shear mode secondary cracks as a cause of rock sample failure under loading. These secondary cracks initiate at the same stresses as wing cracks during uniaxial compression. However, at elevated confining pressure, Bobet (2000) does not observe wing cracks to initiate at all, and only observe secondary cracks. They observe crack coalescence to be produced from the linkage of wing cracks for overlapping flaw geometries (in the direction of loading) but by secondary cracks for nonoverlapping geometries. Therefore, the assumption presented here that sample failure is caused by coalescence of wing cracks is likely to be accurate at low confining pressures and in samples loaded perpendicular to bedding. During experiments conducted at high confining pressures, or with samples loaded parallel to bedding may be more prone to failure due to secondary shear cracks.

### 2.5. Fluid Injection Experimental Method

As with the triaxial experiments, fluid injection were conducted using the “Phoenix” triaxial deformation apparatus. Sample jacketing and confining pressure were applied in the same way as described in section 2.3. At the borehole end of the sample, a brass disk was mounted at the interface between the sample and piston. This disk featured a single concentric O-ring circumscribing the central borehole and was used to form a pressure seal around the borehole. Unlike previous studies by Vinciguerra et al. (2004) and Li et al. (2016), no differential axial stress was required to maintain this seal.

Experiments were conducted under hydrostatic confinement ( $\sigma_1 = \sigma_2 = \sigma_3$ ), with no differential axial stress applied. As with the triaxial experiments, the samples were not stress-cycled to a higher confining pressure prior to the experiments, and no friction reducing material was used on the interface between sample and piston.

A low-viscosity ( $2.4 \times 10^{-2}$  Pa-s) synthetic ester (Rheolube DOS<sup>®</sup> Di-ethylhexyl sebacate) fluid was injected into the borehole of each sample. In each experiment, the borehole pressure was initially raised rapidly to meet the confining pressure. Air was not specifically removed from the borehole prior to fluid injection. Once the injection and confining pressures were equivalent, injection was continued at a constant volume rate of  $0.1 \text{ mm}^3/\text{min}$  until breakdown, at which point the borehole pressure would fall rapidly to approximately the confining pressure. Here, injection volume rate was not investigated, but the materials tested here are 2–3 orders of magnitude less permeable than those tested by Zoback et al., so no dependence should be expected. A second series of experiments was conducted in the Pennant sandstone with a much higher-viscosity  $2 \times 10^3$ -Pa-s silicone oil fluid in order to investigate the effect of fluid viscosity. A constant volume injection rate was used in all injection experiments to control the fluid injection rather than a constant pressurization rate. This was expected to ensure that the breakdown pressure was independent of pressurization rate, following Zoback et al. (1977) who suggest that the dependence on rate that they observe in constant pressurization rate experiments was caused by diffusion of the injection fluid into the samples at lower pressurization rates. It might be expected that this effect would be significantly smaller for the materials tested here, which have permeabilities on the order of  $10^{-19} \text{ m}^2$  (Rutter & Hackston, 2017), as opposed to the  $\approx 10^{-16} \text{ m}^2$  of the materials tested by Zoback et al.

### 2.6. Determination of Initial Flaw Size From Fluid Injection Experiments

Abou-Sayed et al. (1978) derived the stress intensity at the tip of a preexisting flaw in the wall of a two-dimensional borehole, for a situation where there are two independent horizontal stresses,  $\sigma_2$  and  $\sigma_3$ . In the case that the horizontal stress is uniform ( $\sigma_2 = \sigma_3$ ), the orientation of the flaw is unimportant, and the solution is therefore simplified considerably. Figure 3a shows the situation described, with  $r_{\text{bore}}$  being the borehole radius and  $l_{\text{flaw}}$  the initial flaw length. Assuming that breakdown occurs when the stress intensity reaches the fracture toughness (i.e.,  $K_I = K_{Ic}$ ), and substituting  $\sigma_2 = \sigma_3$  into the solution derived by Abou-Sayed et al. (1978), the fracture toughness is found to be given by

$$K_{Ic} = (P_{\text{breakdown}} - \sigma_3) (F(\beta)(\pi l_{\text{flaw}})^{1/2}), \quad (12)$$

where  $F$  is a known function of the dimensionless crack length,  $\beta = l_{\text{flaw}}/r_{\text{bore}}$ , which is tabulated by Paris and Sih (1965) and Abou-Sayed et al. (1978).  $F$  is tabulated separately for cases where the borehole wall has two flaws (as shown in Figure 3a) or a single flaw.

The fractures observed on the flat surface of each postexperiment sample were seen to be one sided (as seen in Figure 3b); hence, the single crack form of  $F(\beta)$  from Abou-Sayed et al. (1978) was used for all experiments.  $K_{Ic}$  values for each material were taken from Chandler et al. (2018) and are listed in Table 4.



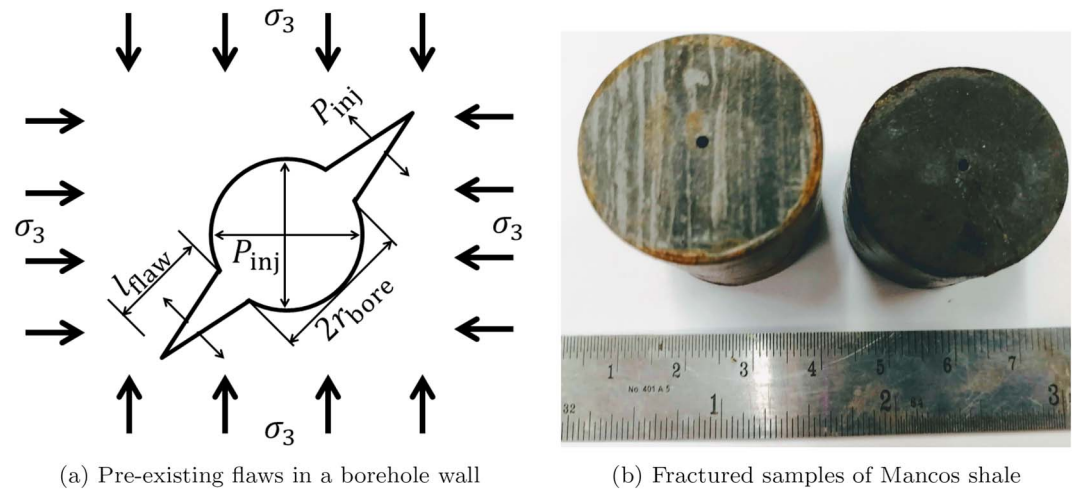


**Figure 3.** (a) Preexisting flaws in a borehole wall, following the analysis of Abou-Sayed et al. (1978). A circular borehole of radius  $r_{\text{bore}}$  has notches of length  $l_{\text{flaw}}$  extending radially from the borehole wall. The borehole (and notches) are pressurized by a fluid pressure,  $P_{\text{inj}}$ . The configuration shown here corresponds to two radial cracks in the borehole wall and a uniform horizontal stress,  $\sigma_3$ . Figure is modified after Abou-Sayed et al. (1978). (b) Photograph of samples of Mancos shale after a fluid injection experiments.

Each fluid injection experiment provides a value for both  $P_{\text{breakdown}}$  and  $\sigma_3$ , so for a borehole of known radius in a material of known  $K_{Ic}$ , each experiment can be used to find an initial flaw length,  $l_{\text{flaw}}$  by rearranging equation (12) into the form

$$l_{\text{flaw}} = \left( \frac{K_{Ic}}{[P_{\text{breakdown}} - \sigma_3] F(\beta) \sqrt{\pi}} \right)^2 \quad (13)$$

This analysis assumes that the flaws in question lie parallel to the initial borehole and that the vertical stress ( $\sigma_1$ ) has no effect on the fracture propagation. The simplification of the geometry to two dimensions follows Stoeckhert et al. (2014) and essentially assumes that the extension of the initial flaw in the third dimension along the length of the borehole requires a negligible amount of energy compared to that expended in lengthening the fracture away from the borehole. It is likely that this extension along the borehole length does require less energy than extension radially away from the borehole, because the circumferential stress caused by the pressurized borehole will have a greater influence in the region closer to the borehole. However, no attempt to quantify this difference has been made. Once the crack has ceased propagation in this borehole-parallel direction, the extent of the initial flaw in this dimension should not be expected to have a significant effect on this analysis, as the crack opening force is provided by a fluid pressure. The applied force will therefore scale in direct proportion to the crack width, so the problem can be approximated to two-dimensional as long as the crack length is reasonably constant along its entire width, and the flaw lies parallel to the borehole. The  $\sigma_1$  may, however, be expected to affect the hoop stress through the effect of Poisson's ratio, so the values of  $l_{\text{flaw}}$  derived through equation (13) should be thought of as minimum values.

### 3. Results

#### 3.1. Triaxial Experimental Results

Table 2 lists the experimental results from the triaxial experiments. The Young's modulus,  $E$ , was determined from the gradient of the linear region of the differential stress-axial strain curves. A 50-mm-long steel dummy specimen was used to confirm the accuracy of  $E$  values determined this way. This calibration was conducted at 25, 45, and 80 MPa and found  $E$  to lie within 10% of the manufacturer quoted value. The onset of nonlinearity was picked by eye and corresponds to the points in the stress-strain curves when the curve ceases to increase linearly. Figure 4 shows the axial failure stress and axial stress at the onset of nonlinearity as a function of confining pressure.

**Table 2**  
*Summary of Triaxial Experiments*

| Material             | $\sigma_1$ Orientation   | $\sigma_3$<br>(MPa) | $P_{\text{pore}}$<br>(MPa) | $P_{\text{eff}}$<br>(MPa) | $E$<br>(GPa) | $\sigma_{1,\text{fail}}$<br>(MPa) | $\sigma_{1,\text{nonlinearity}}$<br>(MPa) |       |       |
|----------------------|--------------------------|---------------------|----------------------------|---------------------------|--------------|-----------------------------------|---|-------|-------|
| Whitby<br>mudstone   | Bedding                  | 4.4                 | 0.0                        | 4.4                       | 12.6         | 56.9                              | 50.5                                      |       |       |
|                      |                          | 13.5                | 0.0                        | 13.5                      | 11.6         | 69.2                              | 66.6                                      |       |       |
|                      |                          | 28.9                | 0.0                        | 28.9                      | 15.1         | 107.0                             | 100.2                                     |       |       |
|                      |                          | 43.6                | 0.0                        | 43.6                      | 16.3         | 116.6                             | 105.8                                     |       |       |
|                      |                          | 59.4                | 0.0                        | 59.4                      | 18.2         | 169.3                             | 143.6                                     |       |       |
|                      | 83.5                     | 0.0                 | 83.5                       | 1.9                       | 196.8        | 170.7                             |   |       |       |
|                      | perpendicular            | 3.9                 | 0.0                        | 3.9                       | 8.4          | 56.1                              | 54.3                                      |       |       |
|                      |                          | 14.6                | 0.0                        | 14.6                      | 8.4          | 84.2                              | 71.2                                      |       |       |
|                      |                          | 29.1                | 0.0                        | 29.1                      | 10.0         | 127.7                             | 114.1                                     |       |       |
|                      |                          | 44.1                | 0.0                        | 44.1                      | 11.1         | 143.5                             | 127.0                                     |       |       |
|                      |                          | 58.6                | 0.0                        | 58.6                      | 11.6         | 174.4                             | 155.2                                     |       |       |
|                      |                          | Mancos<br>shale     | Bedding<br>parallel        | 8.2                       | 0.0          | 8.2                               | 32.1                                      | 127.0 | 106.7 |
|                      |                          |                     |                            | 28.1                      | 0.0          | 28.1                              | 42.4                                      | 161.2 | 128.2 |
|                      |                          |                     |                            | 49.6                      | 0.0          | 49.6                              | 45.9                                      | 195.6 | 153.9 |
| 68.0                 |                          |                     |                            | 0.0                       | 68.0         | 42.6                              | 208.2                                     | 168.8 |       |
| 88.5                 | 0.0                      |                     |                            | 88.5                      | 57.7         | 235.6                             | 203.1                                     |       |       |
| perpendicular        | 8.7                      |                     | 0.0                        | 8.7                       | 16.6         | 99.6                              | 87.0                                      |       |       |
|                      | 28.2                     |                     | 0.0                        | 28.2                      | 32.9         | 138.6                             | 110.0                                     |       |       |
|                      | 51.0                     |                     | 0.0                        | 51.0                      | 34.7         | 189.2                             | 147.7                                     |       |       |
|                      | 68.4                     |                     | 0.0                        | 68.4                      | 39.9         | 200.3                             | 162.0                                     |       |       |
|                      | 88.6                     |                     | 0.0                        | 88.6                      | 30.0         | 248.0                             | 184.3                                     |       |       |
| Pennant<br>sandstone | Bedding<br>perpendicular | 38.7                | 0.0                        | 38.7                      | 23.6         | 266.8                             | 241.8                                     |       |       |
|                      |                          | 43.9                | 0.0                        | 43.9                      | 24.3         | 245.1                             | 222.1                                     |       |       |
|                      |                          | 56.8                | 0.0                        | 56.8                      | 29.3         | 311.1                             | 292.1                                     |       |       |
| Penrhyn<br>slate     | Cleavage<br>parallel     | 8.4                 | 0.0                        | 8.4                       | 36.4         | 177.8                             | 177.8                                     |       |       |
|                      |                          | 28.5                | 0.0                        | 28.5                      | 37.2         | 217.8                             | 209.2                                     |       |       |
|                      |                          | 43.6                | 0.0                        | 43.6                      | 38.7         | 253.0                             | 240.3                                     |       |       |
|                      |                          | 58.4                | 0.0                        | 58.4                      | 48.1         | 269.6                             | 248.1                                     |       |       |
|                      |                          | 59.3                | 0.0                        | 59.3                      | 36.9         | 350.3                             | 350.3                                     |       |       |
|                      |                          | 119.6               | 0.0                        | 119.6                     | 43.2         | 597.1                             | 570.5                                     |       |       |
|                      | perpendicular            | Cleavage            | 3.4                        | 0.0                       | 3.4          | 21.1                              | 262.2                                     | 262.2 |       |
|                      |                          | 14.6                | 0.0                        | 14.6                      | 23.2         | 300.1                             | 300.1                                     |       |       |
|                      |                          | 28.7                | 0.0                        | 28.7                      | 25.0         | 347.7                             | 347.7                                     |       |       |
|                      |                          | 87.4                | 0.0                        | 87.4                      | 36.9         | 578.8                             | 391.8                                     |       |       |
|                      |                          | 119.8               | 0.0                        | 119.8                     | 35.7         | 678.0                             | 678.0                                     |       |       |

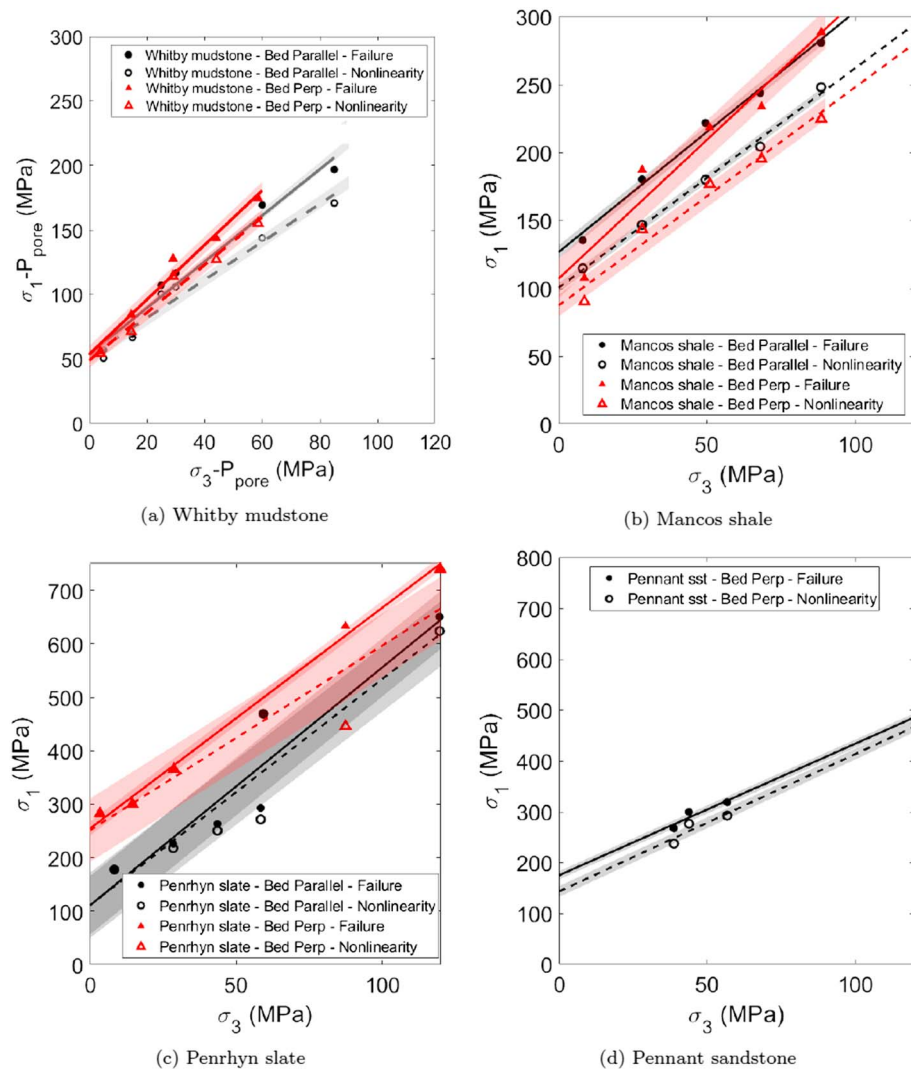
### 3.2. Fluid Injection Experimental Results

Table 3 lists the experimental results from the fluid injection experiments. Figure 5 shows an example plot of injection pressure as a function of injected volume. Figure 6 shows breakdown pressures as a function of confining pressure for each material.

## 4. Discussion

### 4.1. Anisotropy in Failure Strength and Stress at Onset of Nonlinearity in Triaxial Experiments

Table 4 lists parameters including the uniaxial compressive strength  $\sigma_c$  and cohesion,  $C$ , determined from linear least squares fits to the failure stresses as a function of the confining pressures, alongside their corresponding  $R^2$  values.



**Figure 4.** Peak axial stress (solid points) and axial stress at the point of deviation from linearity (hollow points), as a function of confining pressure for triaxial experiments conducted at confining pressures between 5 and 90 MPa. Experiments were conducted on Whitby mudstone (a), Mancos shale (b), Penrhyn slate (c), and Pennant sandstone (d). In each case the black data have  $\sigma_1$  (and the cylinder axis) oriented layering parallel, and the red data have  $\sigma_1$  oriented layering perpendicular. The shaded region around each line corresponds to the root-mean-square uncertainty in  $\sigma_1$ , and the  $R^2$  values associated with the failure stresses are listed in Table 4.

Intact rock shear failure strengths for samples loaded parallel and perpendicular to bedding are generally assumed to be the same in cases where anisotropic rock strength is caused by a single plane of weakness (Paterson & Wong, 2005; Sone & Zoback, 2013). In the case of shales, the bedding planes provide such a plane of weakness, but due to the anisotropic nature of the shale matrix, it is worth investigating the failure strengths of the bedding-parallel and bedding-perpendicular samples separately. McLamore and Gray (1967), Sone and Zoback (2013), and Bonnelye et al. (2017) all find samples of shales to support a slightly higher maximum differential stress in the bedding-parallel orientation than in the bedding-perpendicular orientation over a range of confining pressures. Ambrose (2014) found the same in Bossier shale but found no difference between the two orientations in the Vaca Muerta shale. Ambrose (2014) additionally conducted triaxial experiments at a range of intermediate angles to bedding, finding that the shear strength falls between the two axes, reaching a nadir at 60° to bedding perpendicular. In the shales tested here, the failure stresses measured in the bedding-parallel and bedding-perpendicular orientations are very similar.

Hackston and Rutter (2016) found a substantially steeper dependence of  $\sigma_{1, fail}$  on  $\sigma_3$  in Pennant sandstone than is observed here. The trend presented here in Pennant sandstone was determined from only three

**Table 3**  
*Summary of Fluid Injection Experiments*

| Material        | Borehole orientation   | $\nu_{inj}$<br>(Pa · s) | $\sigma_3$<br>(MPa)   | $P_{breakdown}$<br>(MPa) |
|-----------------|------------------------|-------------------------|-----------------------|--------------------------|
| Whitby mudstone | Bedding perpendicular  | $10^{-2}$               | 19.5                  | 50.8                     |
|                 |                        | $10^{-2}$               | 38.0                  | 107.9                    |
|                 |                        | $10^{-2}$               | 39.4                  | 71.0                     |
|                 |                        | $10^{-2}$               | 58.7                  | 130.4                    |
|                 |                        | $10^{-2}$               | 59.5                  | 108.3                    |
|                 |                        | $10^{-2}$               | 79.8                  | 118.4                    |
| Mancos shale    | Bedding parallel       | $10^{-2}$               | 98.4                  | 151.8                    |
|                 |                        | $10^{-2}$               | 29.0                  | 36.0                     |
|                 |                        | $10^{-2}$               | 38.4                  | 44.8                     |
|                 |                        | $10^{-2}$               | 59.6                  | 98.1                     |
|                 |                        | $10^{-2}$               | 78.1                  | 125.7                    |
|                 |                        | $10^{-2}$               | 98.9                  | 141.6                    |
| Mancos shale    | Bedding perpendicular  | $10^{-2}$               | 99.6                  | 111.8                    |
|                 |                        | $10^{-2}$               | 18.4                  | 24.4                     |
|                 |                        | $10^{-2}$               | 39.1                  | 60.0                     |
|                 |                        | $10^{-2}$               | 59.4                  | 77.6                     |
|                 |                        | $10^{-2}$               | 78.6                  | 94.3                     |
|                 |                        | $10^{-2}$               | 98.3                  | 121.5                    |
| Penrhyn slate   | Cleavage perpendicular | $10^{-2}$               | 18.3                  | 67.5                     |
|                 |                        | $10^{-2}$               | 39.6                  | 76.6                     |
|                 |                        | $10^{-2}$               | 56.4                  | 102.8                    |
|                 |                        | $10^{-2}$               | 78.9                  | 181.5                    |
|                 |                        | $10^{-2}$               | 98.0                  | 164.8                    |
|                 |                        | Pennant sandstone       | Bedding perpendicular | $10^{-2}$                |
| $10^{-2}$       | 19.4                   |                         |                       | 48.7                     |
| $10^{-2}$       | 21.3                   |                         |                       | 51.8                     |
| $10^{-2}$       | 28.8                   |                         |                       | 51.9                     |
| $10^{-2}$       | 29.5                   |                         |                       | 59.5                     |
| $10^{-2}$       | 39.5                   |                         |                       | 83.9                     |
| $10^{-2}$       | 43.5                   |                         |                       | 106.6                    |
| $10^{-2}$       | 50.4                   |                         |                       | 101.5                    |
| $10^{-2}$       | 58.2                   |                         |                       | 109.6                    |
| $10^{-2}$       | 59.1                   |                         |                       | 103.1                    |
| $10^{-2}$       | 68.8                   |                         |                       | 102.8                    |
| $10^{-2}$       | 79.8                   |                         |                       | 125.9                    |
| $10^{-2}$       | 99.5                   |                         |                       | 155.9                    |
| $2 \times 10^3$ | 18.9                   |                         |                       | 43.8                     |
| $2 \times 10^3$ | 39.1                   | 113.1                   |                       |                          |
| $2 \times 10^3$ | 58.9                   | 120.1                   |                       |                          |
| $2 \times 10^3$ | 78.5                   | 154.8                   |                       |                          |
| $2 \times 10^3$ | 99.1                   | 160.5                   |                       |                          |

Note.  $\nu_{inj}$  is the viscosity of the injected fluid.

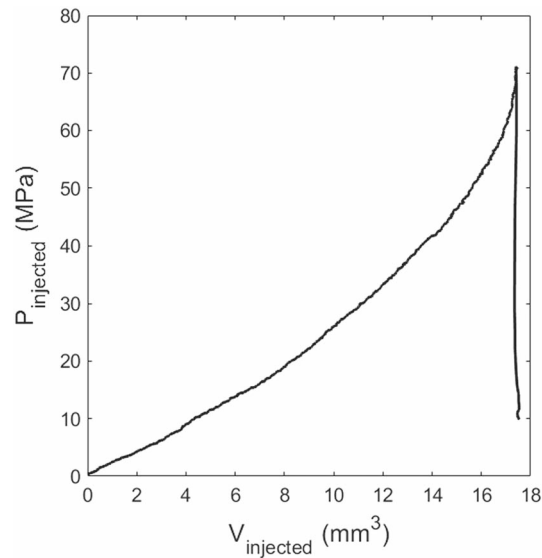


**Figure 5.** Injection pressure as a function of injected volume of fluid viscosity  $2.4 \times 10^{-2}$  Pa·s, for a fluid injection experiment conducted in Whitby mudstone at 40-MPa confining pressure. The final stress drop corresponds to breakdown of the sample, as a fracture reaches the sample surface.

experiments conducted at confining pressures between 38 and 57 MPa and is associated with a low  $R^2$  value of 0.67. Therefore, the triaxial results in Pennant sandstone are much less well constrained than in the other materials tested here but are included for comparison with the fluid injection experiments.

In the Penrhyn slate, failure stresses in the cleavage-perpendicular orientation are significantly higher than in the cleavage-parallel orientation. This agrees with the results of Donath (1972) in Martinsburg slate. This anisotropy is likely due to the increased difficulty in the formation of microcracks perpendicular to cleavage. However, this is the opposite of the trend observed in an unnamed slate by McLamore and Gray (1967), who found a slightly higher failure stress in the cleavage-parallel orientation.

#### 4.2. Flaw Sizes Determined Using the Wing Crack Model of Triaxial Failure

Table 4 lists all of the standard parameters determined from the triaxial experiments using the Mohr-Coulomb analysis described in section 2.3, as well as those additional parameters derived from the wing crack analysis presented in section 2.4. Table 4 additionally lists average grain sizes,  $\bar{d}_{\text{grain}}$ , for each

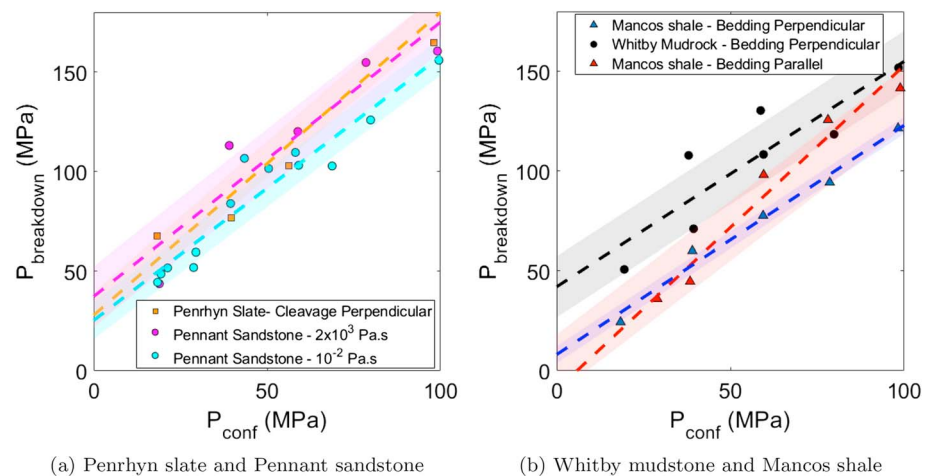


**Figure 6.** Breakdown pressure,  $P_{\text{breakdown}}$ , as a function of confining pressure for samples of Penrhyn slate and Pennant sandstone (a), and for samples of Whitby mudstone and Mancos shale, in bedding-perpendicular and bedding-parallel orientations (b). For the Pennant sandstone, two fluid viscosities are shown. The shaded region around each line corresponds to the root-mean-square uncertainty in  $P_{\text{breakdown}}$ .

**Table 4**

Parameters Derived From Triaxial Experiments, Following the Standard Triaxial Method as Described by Zhao (2000) and the Wing Crack Model Following Bonnelye et al. (2017)

| Parameter  | Units   | Whitby mudstone   |                       | Mancos shale      |                       | Penrhyn slate     |                        | Pennant sandstone     |
|------------|---------|-------------------|-----------------------|-------------------|-----------------------|-------------------|------------------------|-----------------------|
|            |         | Bedding parallel  | Bedding perpendicular | Bedding parallel  | Bedding perpendicular | Cleavage parallel | Cleavage perpendicular | Bedding perpendicular |
| $\phi$     | Radians | $0.30 \pm 0.05$   | $0.37 \pm 0.07$       | $0.14 \pm 0.04$   | $0.29 \pm 0.05$       | $0.63 \pm 0.14$   | $0.61 \pm 0.02$        | $0.52 \pm 0.41$       |
| $\mu_s$    |         | $0.31 \pm 0.06$   | $0.38 \pm 0.08$       | $0.14 \pm 0.04$   | $0.30 \pm 0.06$       | $0.73 \pm 0.22$   | $0.61 \pm 0.03$        | $0.56 \pm 0.38$       |
| $C$        | MPa     | $17.7 \pm 2.6$    | $18.4 \pm 2.5$        | $52.9 \pm 3.2$    | $32.4 \pm 3.0$        | $26.8 \pm 8.1$    | $64.9 \pm 1.7$         | $39.8 \pm 16.3$       |
| $\sigma_c$ | MPa     | $47.9 \pm 6.7$    | $53.5 \pm 6.9$        | $121.5 \pm 5.7$   | $87.0 \pm 7.6$        | $105.6 \pm 31.0$  | $248.0 \pm 5.8$        | $174.7 \pm 15.8$      |
| $\mu_i$    |         | $0.21 \pm 0.04$   | $0.31 \pm 0.05$       | $0.08 \pm 0.03$   | $0.11 \pm 0.03$       | $0.70 \pm 0.08$   | $0.76 \pm 0.18$        | $0.63 \pm 0.31$       |
| $2a$       | mm      | $0.023 \pm 0.008$ | $0.019 \pm 0.003$     | $0.012 \pm 0.001$ | $0.038 \pm 0.027$     | $0.028 \pm 0.007$ | $0.030 \pm 0.001$      | $0.065 \pm 0.010$     |
| $R^2$      |         | 0.98              | 0.98                  | 0.98              | 0.98                  | 0.93              | 0.99                   | 0.67                  |

Note. The listed  $R^2$  value is that of the linear fits to the data shown in Figure 4. Uncertainties were generated through standard uncertainty propagation of the uncertainties on  $\sigma_c$  and  $\tan(\zeta)$  found through a least squares regression through the data.

material. It might be reasonably assumed that the dimensions of the flaws within the material will scale with the grain dimensions (e.g., Wong & Baud, 1999). In the two shales, the initial flaw sizes,  $2a$ , are seen to correspond closely with the silt grain sizes, but equally in the nonshales,  $2a$  is much shorter than the grain scales.

According to the wing crack model, bulk failure is caused by a critical density of flaws connecting and forming a fault. Therefore, the coefficient of sliding friction on the fault might differ from that on each individual flaw, so that  $\mu_s \neq \mu_i$ . In actuality,  $\mu_s$  and  $\mu_i$  agree reasonably closely in all materials tested here (Table 4), except for Whitby mudstone in the bedding-perpendicular orientation where  $\mu_i \ll \mu_s$ . The flaws within the Whitby mudstone and Mancos shale have a preferred orientation, as shown by Chandler et al. (2017). However, no discrepancy between  $\mu_s$  and  $\mu_i$  is observed in Mancos shale, and therefore, a preferred orientation of flaw does not explain the discrepancy between  $\mu_s$  and  $\mu_i$  in Whitby mudstone.

#### 4.3. Physical Form of the Fluid Injection Fractures and Comparison With Existing Literature Fluid Injection Data

In each fluid injection experiment conducted here, a single-sided borehole-parallel fracture was observed on the flat surface of the cylindrical sample as shown in Figure 3b. While the fractures were easily observed on the cylinder ends, the fractures were very difficult to observe on the curved outer surface of the sample, so it is not known whether there were secondary, borehole-perpendicular fractures generated during some experiments. While linking shear mode fractures similar to those observed by Rutter and Mecklenburgh (2017) were not observable here, this could be due to the much smaller diameter of the samples used here making the offsets much smaller. A further study of the forms of these fractures using X-ray tomography is currently ongoing.

Furthermore, in each material and orientation tested here, the same linear increase in  $P_{\text{injected}}$  with  $V_{\text{injected}}$ , and rapid breakdown was observed. The distinct initiation and breakdown observed by Zoback et al. (1977) and Stanchits et al. (2015) was not observed in our experiments with high-viscosity fluid. Ishida et al. (2004) and Li et al. (2016) also did not observe this distinction, and this may be due to the small scale of the samples used.

#### 4.4. Theoretical Models for the Dependence of Breakdown Pressure on Confining Pressure During Fluid Injection Experiments

Figure 7 shows the breakdown pressure data from both orientations in Mancos shale compared to the models of Hubbert and Willis (1972), Haimson and Fairhurst (1967), and Ito and Hayashi (1991; from equations (2), (3), and (5), respectively). The data are the same as plotted in Figure 6b. It can be seen that all of the models

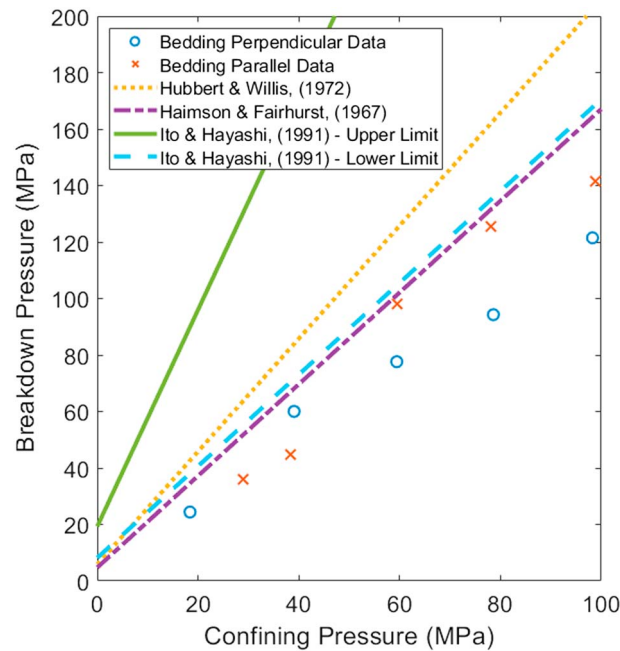


**Figure 7.** Breakdown pressure data for Mancos shale compared to the models of Hubbert and Willis (1972) and Haimson and Fairhurst (1967) and the lower and upper limits of the model proposed by Ito and Hayashi (1991). These models are given by equations (2), (3), and (5), respectively. Plots for the other materials tested here are not included here but demonstrated the same trends. The values of  $K_{IC}$  used in plotting these models are listed in Table 1. The values of  $\sigma_T$  are from Chandler et al. (2016).

predict a greater dependence on confining pressure than the data demonstrates. This discrepancy was also observed in all of the other materials tested here.

For the model of Ito and Hayashi (1991), the  $\sigma_T$  values were taken from Chandler et al. (2016). McKernan et al. (2017) found a mean value of  $\alpha = 0.71 \pm 0.22$  in Whitby mudstone during permeability measurements, and values of  $\approx 0.7$  were assumed in the other materials tested here. In our experiments  $\sigma_2 = \sigma_3$  and  $P_{\text{pore}} = 0$ , and the breakdown pressure according to Hubbert and Willis or Haimson and Fairhurst (from equations (2) and (3), respectively) should therefore be purely a function of the confining pressure for a material of known  $\sigma_T$ ,  $\nu$ , and  $\alpha$ . The permeability of these materials is extremely low (on the order of  $10^{-18}$ – $10^{-19} \text{ m}^2$ ) so the assumptions behind equation (2) are expected to be valid. The models of Detournay and Cheng (1992), Song et al. (2001), Detournay and Carbonell (1997), and Zhang et al. (2017) are not plotted here as they require the determination of parameters that are outside the scope this study.

#### 4.5. Flaw Sizes Determined From Fluid Injection Experiments

Figure 8 shows the variation of flaw sizes determined during fluid injection experiments, as a function of confining pressure for each material. In Pennant sandstone and Penrhyn slate, flaw sizes around 0.02 mm were found at low confining pressures, falling to  $\approx 0.005$  mm as confining pressure rises above 40 MPa. In the two shales, flaw sizes around 0.01 mm were found throughout the range of confining pressures.

In the Pennant sandstone, identical injection experiments were conducted using two different viscosities of fluid. The  $2.4 \times 10^{-2}$ -Pa-s ester fluid employed in all other tests was used, and an additional set of experiments was conducted using a  $2 \times 10^3$ -Pa-s silicone oil. Figure 8d shows the derived flaw length as a function of confining pressure for Pennant sandstone with the two different fluids. At confining pressures above  $\approx 40$  MPa the low-viscosity fluid appears to encounter a  $\approx 2$ - $\mu\text{m}$  longer flaw than does the high-viscosity fluid. This effect is very small but could be interpreted as the same population of flaws but with the higher-viscosity fluid being unable to reach the entire way into the flaw. This type of lag between the fluid front and the tip of a fracture has been shown to have a large effect on the propagation regime of a fluid-driven fracture by Garagash and Detournay (2000), who identify distinct “viscosity dominated” and “toughness dominated” propagation regimes for fluid-driven fractures.

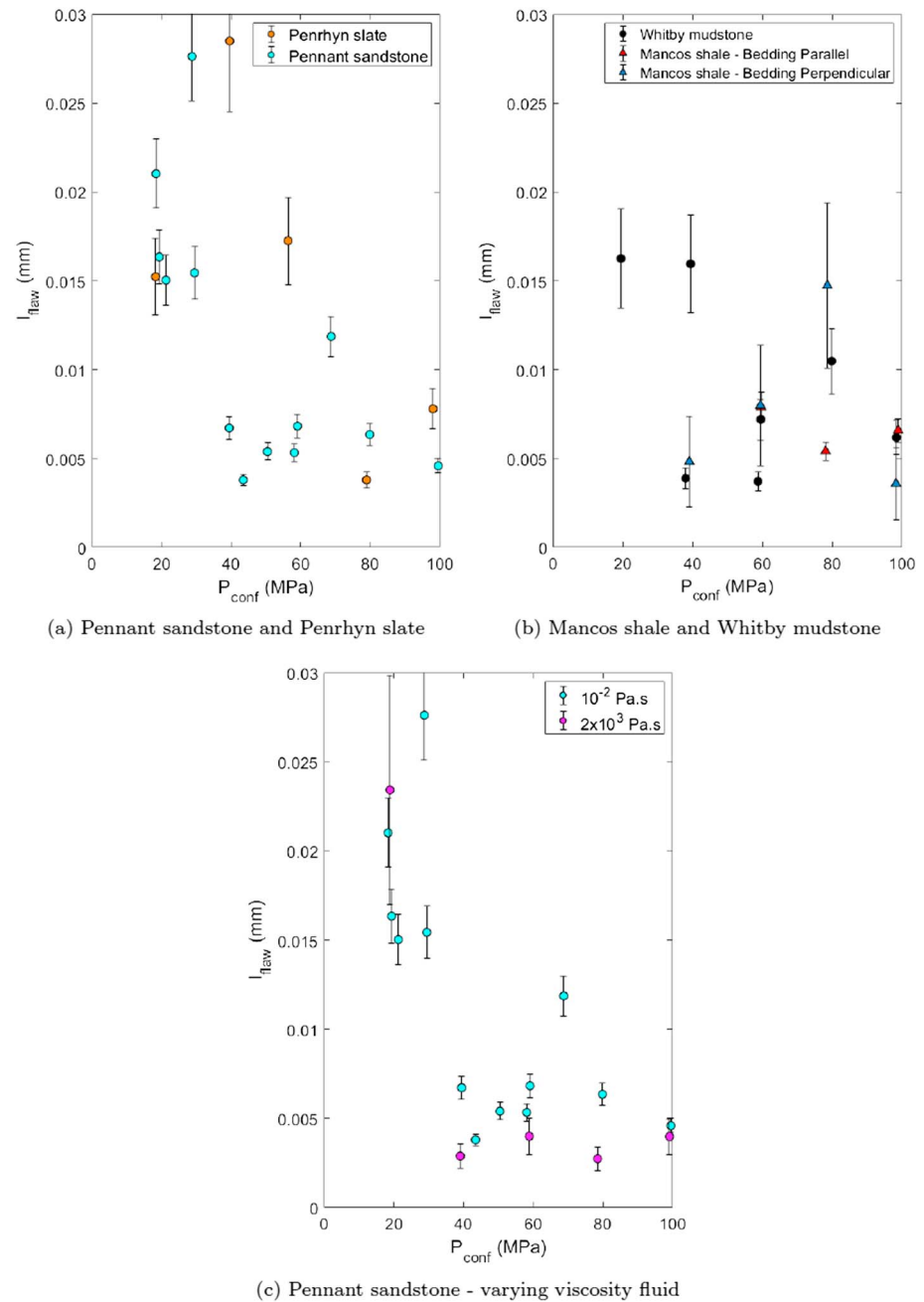


**Figure 8.** (a and b) Flaw lengths as a function of confining pressure, derived from the fluid injection experiments conducted on (a) Penrhyn slate and Pennant sandstone and (b) Whitby mudstone and Mancos shale. (c) Flaw lengths as a function of confining pressure, derived from the fluid injection experiments conducted on Pennant sandstone with injected fluids of two different viscosities.

#### 4.6. Comparison Between the Flaw Sizes Derived From the Triaxial and Fluid Injection Experiments

Initial flaw sizes derived from triaxial experiments are listed in Table 4. Initial flaw sizes derived from fluid injection experiments are plotted in Figures 8b–8d.

In the nonshale materials, there is a reasonable agreement between the flaw sizes derived from the triaxial data and those derived from the fluid injection experiments conducted at low confining pressures. Neither derived flaw size are particularly close to the grain diameters of the material, as listed in Table 1. At confining pressures above  $\approx 30$  MPa, the fluid injection experiments display a shorter initial flaw size. Figure 8d



shows that a slightly shorter flaw size is observed in this range when using a lower-viscosity fluid. This might suggest that each failure mode is controlled by the same population of flaws but that during fluid injections at confining pressures greater than  $\approx 30$  MPa, the confining pressure is able partially to close up the initial flaws. The low-viscosity fluid is able to reach slightly further into these partially closed flaws than the higher-viscosity fluid.

In the shale materials, the flaw sizes derived from triaxial experiments are longer than those derived from the fluid injection experiments. Flaw sizes derived from triaxial experiments lie in the region of 15–40  $\mu\text{m}$ , which is a similar range to the silt grain sizes. Flaw sizes derived from the fluid injection experiments are around 5–15  $\mu\text{m}$ . Here, the type of feature that will act as a flaw for these two types of experiment should be considered. In a fluid injection experiment a flaw must be able to open in mode-I, either by the fluid directly accessing the flaw or opening due to the circumferential stress around the pressurized borehole. These two possibilities are equivalent to the slow and fast pressurization cases defined by Ito and Hayashi (1991). During axial compression the initial flaw can be any sliding contact. There is no requirement that the initial flaw must be open during a triaxial experiment, as it moves in shear, during compression. Therefore, the discrepancy between the large flaw sizes derived for the shales in triaxial experiments and the shorter flaws derived from the fluid injection experiments could be seen as evidence of two populations of flaws within the materials. A population of long but closed flaws controls triaxial failure but is inaccessible to the fluid during injection experiments. A second population of shorter, but open flaws controls breakdown during the fluid injection.

In the triaxial experiments, a mean flaw length of  $2\bar{a} = 0.024 \pm 0.010$  mm was measured in the shales, while the equivalent mean length in the nonshales was  $2\bar{a} = 0.042 \pm 0.009$  mm. The uncertainty is high, but this corresponds to a ratio of 0.56:1, with the shales having a mean flaw length approximately half of that determined in the nonshales. Through equation (1), this suggests that  $\sigma_T$  should be more dependent on  $K_{Ic}$  in shales by a factor of  $\approx \sqrt{2}$ . In fact, the results plotted in Figure 1 suggest a larger difference, of  $\approx 2$  although again, the uncertainties involved are large.

Flaw sizes calculated through both methods rely on the assumption that  $K_{Ic}$  does not vary as a function of confining pressure. Various studies including Schmidt and Huddle (1977) and Stoeckhert et al. (2016) have suggested that  $K_{Ic}$  may increase linearly as a function of confining pressure. Yew and Liu (1993) and Khazan and Fialko (1995) suggest that this increase could be caused by inhibition of the dilatation within the inelastic zone. If this is the case, then through equation (13), the reduction in  $l_{\text{flaw}}$  with confining pressure would be significantly lower during fluid injection experiments. If  $K_{Ic}$  increases with confining pressure, then some component of the experimentally observed increase in  $\sigma_1$  with  $\sigma_3$  during triaxial experiments will be caused by the increase in  $K_{Ic}$ . Therefore, through equation (11), this would imply lower values of  $\mu_i$  and  $a$ .

## 5. Conclusions

A suite of triaxial deformation experiments and direct fluid injection experiments have been conducted at confining pressures up to 100 MPa, on samples of Mancos shale, Whitby mudstone, Penrhyn slate, and Pennant sandstone.

Triaxial failure stresses were found to be similar between the two orientations in the shale. The similarity between these two orientations does not rule out significantly lower failure stresses at angles intermediate between the two, following the plane-of-weakness model, and similar to the results of Ambrose (2014). In Penrhyn slate, significantly higher failure stresses were observed in the cleavage-perpendicular orientation. In the shale materials, more strain is accumulated for samples manufactured for loading perpendicular to layering than those manufactured for loading parallel to bedding. This is believed to be due to the compression of existing microcracks which are preferentially oriented parallel to bedding, as these samples were not stress-cycled prior to the experiments.

The wing crack model was employed to determine the internal friction coefficient from each series of triaxial experiments, which was found to agree well with the friction coefficient determined using Mohr-Coulomb analysis. Initial flaw size was also calculated using the wing crack model and was found to be in the region of 40  $\mu\text{m}$  for the materials tested here, with the shales demonstrating slightly shorter initial flaws than the nonshales. This agrees broadly with the trend in  $\sigma_T(K_{Ic})$  shown in Figure 1, with the results for shales implying a slightly shorter initial flaw length than a range of other rock types. The flaw sizes determined

for the shales were close to the diameters of the silt grains, while the flaw sizes in the slate and sandstone did not appear to correlate closely with the grain sizes. Further work in adapting this method to account for anisotropically inclined populations of initial flaws could improve the accuracy of this method in anisotropic materials such as shales.

During direct fluid injection experiments with a low-viscosity fluid, breakdown was seen to be rapid and uncontrolled. In Pennant sandstone, a very high viscosity fluid was also trialed, with breakdown still observed to be rapid and uncontrolled. Breakdown pressure increased linearly with confining pressure but was observed to be less sensitive to confining pressure than the models of Hubbert and Willis (1972), Haimson and Fairhurst (1967), and Ito and Hayashi (1991) suggest should be the case. This potentially implies a lower dependence on depth for breakdown pressures measured in field fluid injections, although the relationship is complicated, with fluid pressure equilibration governing a large proportion of energy dissipation at the initiation of hydraulic fractures. A fracture mechanics model based on the work of Abou-Sayed et al. (1978) was proposed to determine the initial flaw size responsible for the breakdown in direct fluid injection experiments. Flaw sizes determined in this way agree with those determined from the triaxial data in the nonshale materials at low confining pressures. As confining pressure rises, a threshold is reached at around 30 MPa, above which the fluid injection experiments suggest a lower initial flaw length of around 10  $\mu\text{m}$ . The threshold in flaw length with confining pressure is interpreted as being due to the partial closure of a population of flaws, restricting the distance to which the injection fluid can reach prior to fracture.

In the shale materials an initial flaw length of around 10  $\mu\text{m}$  was determined from the fluid injection experiments at all confining pressures. This is  $\approx 2.5$  times smaller than that determined from the triaxial experiments. The discrepancy between flaw sizes determined using each method could be interpreted as evidence of two populations of flaws. A first population of long, closed flaws is responsible for the triaxial failure but inaccessible to fluid during injection. A second population of shorter, open flaws could be responsible for failure during fluid injection. While this work provides experimental data and evidence suggesting approximate flaw sizes leading to fracture propagation, further work is required to investigate exactly what features within each material might correspond to these flaws and thereby validate this method. Microscopy studies of the materials could potentially be used to characterize flaw populations, or in situ X-Ray tomography during this type of experiment could help to characterize the locations where fractures nucleate. Additionally, modeling work to extend the 2-D model of fluid injection experiments (as described in section 2.6) into the third dimension would aid significantly in both this type of flaw size analysis and future studies attempting to determine  $K_{Ic}$  from fluid injection.

## Nomenclature

|                            |   |
|----------------------------|---|
| $\alpha$                   | Biot effective stress parameter.  |
| $\beta$                    | Dimensionless crack length, $\beta = l_{\text{flaw}}/r_{\text{bore}}$ .                         |
| $\delta$                   | Diffusion length.   |
| $\delta_{ij}$              | Kronecker delta function.   |
| $\dot{\epsilon}$           | Axial strain rate.  |
| $\epsilon$                 | Axial strain.   |
| $\iota$                    | A dimensionless geometric factor involved in relating stress intensity to a flaw in a material. |
| $\kappa$                   | An effective stress parameter, defined by Schmitt and Zoback (1989).                            |
| $\mu_i$                    | Internal friction coefficient.  |
| $\mu_s$                    | Sliding friction coefficient.   |
| $\nu$                      | Poisson's ratio.  |
| $\nu_{\text{inj}}$         | Viscosity of the injected fluid.  |
| $\bar{d}_{\text{grain}}$   | Average grain diameter.   |
| $\phi_{\text{open}}$       | Open porosity.  |
| $\phi_{\text{total}}$      | Total porosity.   |
| $\psi$                     | Angle between an inclined flaw and the $\sigma_1$ in the wing crack model.                      |
| $\sigma_{ij}^{\text{eff}}$ | Terzaghi effective stress.  |
| $\sigma_1$                 | The highest principal stress.   |
| $\sigma_2$                 | The intermediate principal stress.  |
| $\sigma_3$                 | The lowest principal stress.  |

- $\sigma_C$  Compressive strength.  
 $\sigma_f$  The failure stress of an arbitrary sample.  
 $\sigma_{H,max}$  Maximum horizontal stress.  
 $\sigma_{H,min}$  Minimum horizontal stress.  
 $\sigma_T$  Tensile strength.  
 $\sigma_V$  Vertical stress.  
 $\sigma_\theta$  Circumferential stress.  
 $\sigma_{1,fail}$  Axial stress at failure during a triaxial experiment.  
 $\sigma_{1,nonlinearity}$  Axial stress at the onset of nonlinearity during a triaxial experiment.  
 $\epsilon_{dry}$   $P$  wave anisotropy, as defined in equation (32) of Berryman (2008).  
 $\varphi$  Friction angle.  
 $\zeta$  The tangent to the gradient of a  $\sigma_1(\sigma_3)$  plot from a series of triaxial experiments.  
 $A$  Borehole pressurization rate.  
 $a$  Initial flaw half-length in the wing crack model.  
 $C$  Cohesion, as defined by Zhao (2000).  
 $d$  Characteristic length of tensile failure.  
 $E$  Young's modulus.  
 $F(\beta)$  A known function of  $\beta$ , tabulated by Paris and Sih (1965) and Abou-Sayed et al. (1978).  
 $K_{Ic}$  Mode-I fracture toughness: The critical mode-I stress intensity, above which a fracture propagates.  
 $K_I$  Mode-I stress intensity.  
 $l$  Length of an initiating wing crack.  
 $l_{flaw}$  The initial flaw length during a fluid injection experiment.  
 $P_{breakdown}$  Breakdown pressure (the peak value of  $P_{injected}$ ) during a fluid injection experiment.  
 $P_{conf}$  The confining pressure ( $= \sigma_3$ ).  
 $P_{eff}$  Effective pressure ( $= P_{conf} - P_{pore}$ ).  
 $P_{injected}$  The pressure of the injected fluid, during a fluid injection experiment.  
 $P_{pore}$  Pore pressure.  
 $R^2$  Coefficient of determination.  
 $r_{bore}$  Borehole radius.  
 $S_\theta$  Defined in equation (6).  
 $V_{injected}$  The volume of fluid injected during a fluid injection experiment.  
 $v_p$   $P$  wave velocity measured at 1 MHz.

## Acknowledgments

This work was supported by U.K. Natural Environment Research Council grant NE/M001458/1. The authors would like to thank Steve May for his assistance with the design and maintenance of the equipment used here. The authors would also like to thank John Waters for the XRD analysis of Penrhyn slate. The porosity and ultrasonic  $P$  wave anisotropy in Penrhyn slate was measured by Christopher Brooks, Jack Lartigue, and Henry Tyrrell. Additionally, the authors would like to thank the reviewers and editor whose thorough input has greatly improved the clarity of this study. In accordance with Data Accessibility policy for U.K. Research Council grant-supported research, the data sets used to generate the graphical presentations in this paper are publicly available from the U.K. National Geoscience Data Centre ([www.bgs.ac.uk/services/ngdc](http://www.bgs.ac.uk/services/ngdc)), identified via grant NE/M001458/1.

## References

- Abou-Sayed, A. S., Brechtel, C. E., & Clifton, R. J. (1978). In situ stress determination by hydrofracturing: A fracture mechanics approach. *Journal of Geophysical Research*, *83*(B6), 2851–2862.
- Ambrose, J. (2014). Failure of anisotropic shales under triaxial stress conditions (Ph.D. Thesis), Imperial College London.
- Ashby, M. F., & Hallam, S. D. (1986). The failure of brittle solids containing small cracks under compressive stress states. *Acta Metallurgica*, *34*(3), 497–510.
- Ashby, M. F., & Sammis, C. G. (1990). The damage mechanics of brittle solids in compression. *Pure and Applied Geophysics*, *133*(3), 489–521. <https://doi.org/10.1007/BF00878002>
- Berryman, J. (2008). Exact seismic velocities for transversely isotropic media and extended Thomsen formulas for stronger anisotropies. *Geophysics*, *73*(1), D1–D10. <https://doi.org/10.1190/1.2813433>
- Bobet, A. (2000). The initiation of secondary cracks in compression. *Engineering Fracture Mechanics*, *66*(2), 187–219. [https://doi.org/10.1016/S0013-7944\(00\)00009-6](https://doi.org/10.1016/S0013-7944(00)00009-6)
- Bonnelye, A., Schubnel, A., David, C., Henry, P., Guglielmi, Y., Gout, C., et al. (2017). Strength anisotropy of shales deformed under uppermost crustal conditions. *Journal of Geophysical Research: Solid Earth*, *122*, 110–129. <https://doi.org/10.1002/2016JB013040>
- Bunger, A. P., & Detournay, E. (2008). Experimental validation of the tip asymptotics for a fluid-driven crack. *Journal of the Mechanics and Physics of Solids*, *56*(11), 3101–3115. <https://doi.org/10.1016/j.jmps.2008.08.006>
- Cárdenes, V., Rubio-Ordóñez, Á., Wichert, J., Cnudde, J. P., & Cnudde, V. (2014). Petrography of roofing slates. *Earth-Science Reviews*, *138*, 435–453.
- Chandler, M. R., Fauchille, A.-L., Kim, H. K., Ma, L., Mecklenburgh, J., Rizzo, R., et al. (2018). Correlative optical and X-ray imaging of strain evolution during double-torsion fracture toughness measurements in shale. *Journal of Geophysical Research: Solid Earth*, *123*, 10,517–10,533. <https://doi.org/10.1029/2018JB016568>
- Chandler, M. R., Meredith, P. G., Brantut, N., & Crawford, B. R. (2016). Fracture toughness anisotropy in shale. *Journal of Geophysical Research: Solid Earth*, *121*, 1706–1729. <https://doi.org/10.1002/2015JB012756>
- Chandler, M. R., Meredith, P. G., Brantut, N., & Crawford, B. R. (2017). Effect of temperature on the fracture toughness of anisotropic shale and other rocks. *Geological Society, London, Special Publications*, *454*(1), 295–303. <https://doi.org/10.1144/SP454.6>
- Chen, X., Eichhubl, P., Olson, J. E., & Dewers, T. A. (2019). Effect of water on fracture mechanical properties of shales. *Journal of Geophysical Research: Solid Earth*, *124*, 2428–2444. <https://doi.org/10.1029/2018JB016479>

- Clifton, R. J., Simonson, E. R., Jones, A. H., & Green, S. J. (1976). Determination of the critical-stress-intensity factor  $K_{Ic}$  from internally pressurized thick-walled vessels. *Experimental Mechanics*, 16(6), 233–238.
- Cuss, R. J., Rutter, E. H., & Holloway, R. F. (2003). Experimental observations of the mechanics of borehole failure in porous sandstone. *International Journal of Rock Mechanics and Mining Sciences*, 40(5), 747–761. [https://doi.org/10.1016/S1365-1609\(03\)00068-6](https://doi.org/10.1016/S1365-1609(03)00068-6)
- Detournay, E. (2016). Mechanics of hydraulic fractures. *Annual Review of Fluid Mechanics*, 48(1), 311–339. <https://doi.org/10.1146/annurev-fluid-010814-014736>
- Detournay, E., & Carbonell, R. (1997). Fracture-mechanics analysis of the breakdown process in minifracture or leakoff test. *SPE production & facilities*, 12(03), 195–199.
- Detournay, E., & Cheng, A. (1992). Influence of pressurization rate on the magnitude of the breakdown pressure, *The 33th US Symposium on Rock Mechanics (USRMS)* (pp. 10). New Mexico: American Rock Mechanics Association.
- Donath, F. A. (1972). Effects of cohesion and granularity on deformational behavior of anisotropic rock. *Studies in mineralogy and precambrian geology*, 135, 95–128.
- Dutler, N., Nejati, M., Valley, B., Amann, F., & Molinari, G. (2018). On the link between fracture toughness, tensile strength, and fracture process zone in anisotropic rocks. *Engineering Fracture Mechanics*, 201, 56–79. <https://doi.org/10.1016/j.engfracmech.2018.08.017>
- Forbes Inskip, N. D., Meredith, P. G., Chandler, M. R., & Gudmundsson, A. (2018). Fracture properties of Nash Point shale as a function of orientation to bedding. *Journal of Geophysical Research: Solid Earth*, 123, 8428–8444. <https://doi.org/10.1029/2018JB015943>
- Gao, Y., Liu, Z., Wang, T., Zeng, Q., Li, X., & Zhuang, Z. (2018). Crack forbidden area in the anisotropic fracture toughness medium. *Extreme Mechanics Letters*, 22, 172–175. <https://doi.org/10.1016/j.eml.2018.06.006>
- Garagash, D., & Detournay, E. (2000). The tip region of a fluid-driven fracture in an elastic medium. *Journal of Applied Mechanics*, 67(1), 183–192.
- Hackston, A., & Rutter, E. (2016). The mohr–coulomb criterion for intact rock strength and friction—A re-evaluation and consideration of failure under polyaxial stresses. *Solid Earth*, 7(2), 493–508. <https://doi.org/10.5194/se-7-493-2016>
- Haimson, B., & Fairhurst, C. (1967). Initiation and extension of hydraulic fractures in rocks. *Society of Petroleum Engineers Journal*, 7(03), 310–318.
- Haimson, B. C., & Zhao, Z. (1991). Effect of borehole size and pressurization rate on hydraulic fracturing breakdown pressure. In J. C. Roegiers (Ed.), *The 32nd US Symposium on Rock Mechanics (USRMS)* (pp. 191–199). Oklahoma: American Rock Mechanics Association.
- Hubbert, M. K., & Willis, D. G. (1972). Mechanics of hydraulic fracturing. *M 18: Underground Waste Management and Environmental Implications*, 75, 239–257.
- Ishida, T., Chen, Q., Mizuta, Y., & Roegiers, J.-C. (2004). Influence of fluid viscosity on the hydraulic fracturing mechanism. *Journal of energy resources technology*, 126(3), 190–200.
- Ito, T., & Hayashi, K. (1991). Physical background to the breakdown pressure in hydraulic fracturing tectonic stress measurements. *International Journal of Rock Mechanics and Mining Sciences & Geomechanics Abstracts*, 28(4), 285–293.
- Janssen, M., Zuidema, J., & Wanhill, R. J. H. (2002). *Fracture mechanics* (2nd ed.). Delft, Netherlands: VSSD.
- Khazan, Y. M., & Fialko, Y. A. (1995). Fracture criteria at the tip of fluid-driven cracks in the earth. *Geophysical Research Letters*, 22(18), 2541–2544. <https://doi.org/10.1029/95GL02547>
- Lecampion, B., Desroches, J., Jeffrey, R. G., & Bungler, A. P. (2017). Experiments versus theory for the initiation and propagation of radial hydraulic fractures in low-permeability materials. *Journal of Geophysical Research: Solid Earth*, 122, 1239–1263. <https://doi.org/10.1002/2016JB013183>
- Leckie, R. M., Schmidt, M. G., Finkelstein, D., & Yuretich, R. (1991). Paleoclimatic and paleogeographic interpretations of the Mancos Shale (Upper Cretaceous), Black Mesa Basin, Arizona. *Stratigraphy, Depositional Environments, and Sedimentary Tectonics of the Western Margin, Cretaceous Western Interior Seaway, Geological Society of America Special Paper*, 260, 139–152.
- Lee, H. P., Olson, J. E., Holder, J., Gale, J. F., & Myers, R. D. (2015). The interaction of propagating opening mode fractures with preexisting discontinuities in shale. *Journal of Geophysical Research: Solid Earth*, 120, 169–181. <https://doi.org/10.1002/2014JB011358>
- Li, X., Feng, Z., Han, G., Elsworth, D., Marone, C., Saffer, D., & Cheon, D.-S. (2016). Breakdown pressure and fracture surface morphology of hydraulic fracturing in shale with H<sub>2</sub>O, CO<sub>2</sub> and N<sub>2</sub>. *Geomechanics and Geophysics for Geo-Energy and Geo-Resources*, 2(2), 63–76.
- Lockner, D., & Byerlee, J. D. (1977). Hydrofracture in Weber Sandstone at high confining pressure and differential stress. *Journal of Geophysical Research*, 82(14), 2018–2026.
- Longman, M., & Koepsell, R. (2005). Defining and characterizing Mesaverde and Mancos sandstone reservoirs based on interpretation of formation microimager (FMI) logs, Eastern Uinta Basin, Utah. Open File Report 458 - Utah Geological Survey.
- Luo, Y., Xie, H. P., Ren, L., Zhang, R., Li, C. B., & Gao, C. (2018). Linear elastic fracture mechanics characterization of an anisotropic shale. *Scientific Reports*, 8(1), 8505.
- McCrae, R. W., Powell, D. B., & Yu, H. T. (1979). Engineering geological mapping of large caverns at dinorwic pumped storage scheme, North Wales. *Bulletin of the International Association of Engineering Geology-Bulletin de l'Association Internationale de Géologie de l'Ingénieur*, 19(1), 182–190.
- McKernan, R., Mecklenburgh, J., Rutter, E., & Taylor, K. (2017). Microstructural controls on the pressure-dependent permeability of Whitby mudstone. *Geological Society, London, Special Publications*, 454(1), 39–66.
- McKernan, R. E., Rutter, E. H., Mecklenburgh, J., Taylor, K. G., & Covey-Crump, S. J. (2014). Influence of effective pressure on mudstone matrix permeability: Implications for shale gas production, *Proceedings of SPE/EAGE Conference on Unconventional Reservoirs, Vienna* (pp. 1–13). United States: Society of Petroleum Engineers. <https://doi.org/10.2118/167762-MS>
- McLamore, R., & Gray, K. E. (1967). The mechanical behavior of anisotropic sedimentary rocks. *Journal of Engineering for Industry*, 89(1), 62–73.
- Meier, T., Rybacki, E., Reinicke, A., & Dresen, G. (2013). Influence of borehole diameter on the formation of borehole breakouts in black shale. *International Journal of Rock Mechanics and Mining Sciences*, 62, 74–85. <https://doi.org/10.1016/j.ijrmms.2013.03.012>
- Paris, P. C., & Sih, G. C. (1965). Stress analysis of cracks, *Fracture toughness testing and its applications* (pp. 30–81). West Conshohocken, PA: ASTM International. <https://doi.org/10.1520/STP26584S>
- Paterson, M. S., & Wong, T.-F. (2005). *Experimental rock deformation—The brittle field* (pp. 87). Berlin: Springer.
- Rutter, E., & Hackston, A. (2017). On the effective stress law for rock-on-rock frictional sliding, and fault slip triggered by means of fluid injection. *Philosophical Transactions of the Royal Society A*, 375(2103), 20160001.
- Rutter, E. H., & Mecklenburgh, J. (2017). Hydraulic conductivity of bedding-parallel cracks in shale as a function of shear and normal stress. *Geological Society, London, Special Publications*, 454(1), 67–84. <https://doi.org/10.1144/SP454.9>
- Schmidt, R. A., & Huddle, C. W. (1977). Fracture mechanics of oil shale: Some preliminary results. United States: Sandia Laboratories. <https://doi.org/10.2172/7119762>

- Schmidt, R. A., & Huddle, C. W. (1977). Effect of confining pressure on fracture toughness of Indiana limestone. *International Journal of Rock Mechanics and Mining Sciences & Geomechanics Abstracts*, 14(5-6), 289–293. [https://doi.org/10.1016/0148-9062\(77\)90740-9](https://doi.org/10.1016/0148-9062(77)90740-9)
- Schmitt, D. R., & Zoback, M. D. (1989). Poroelastic effects in the determination of the maximum horizontal principal stress in hydraulic fracturing tests—A proposed breakdown equation employing a modified effective stress relation for tensile failure. *International Journal of Rock Mechanics and Mining Sciences & Geomechanics Abstracts*, 26(6), 499–506.
- Schmitt, D. R., & Zoback, M. D. (1992). Diminished pore pressure in low-porosity crystalline rock under tensional failure: Apparent strengthening by dilatancy. *Journal of Geophysical Research*, 97(B1), 273–288.
- Sone, H., & Zoback, M. D. (2013). Mechanical properties of shale-gas reservoir rocks—Part 2: Ductile creep, brittle strength, and their relation to the elastic modulus. *Geophysics*, 78(5), D393–D402. <https://doi.org/10.1190/geo2013-0051.1>
- Song, I., Suh, M., Won, K. S., & Haimson, B. (2001). A laboratory study of hydraulic fracturing breakdown pressure in Tablerock sandstone. *Geosciences Journal*, 5(3), 263–271. <https://doi.org/10.1007/BF02910309>
- Stanchits, S., Burghardt, J., & Surdi, A. (2015). Hydraulic fracturing of heterogeneous rock monitored by acoustic emission. *Rock Mechanics and Rock Engineering*, 48(6), 2513–2527.
- Stoekherth, F., Brenne, S., Molenda, M., & Alber, M. (2014). Fracture mechanical evaluation of hydraulic fracturing laboratory experiments, *ISRM Regional Symposium-EUROCK 2014* (pp. 1335–1340). Spain: International Society for Rock Mechanics.
- Stoekherth, F., Brenne, S., Molenda, M., & Alber, M. (2016). Mode I fracture toughness of rock under confining pressure. In *Rock Mechanics and Rock Engineering: From the Past to the Future* (pp. 313). Turkey.
- Stoekherth, F., Molenda, M., Brenne, S., & Alber, M. (2015). Fracture propagation in sandstone and slate—laboratory experiments, acoustic emissions and fracture mechanics. *Journal of Rock Mechanics and Geotechnical Engineering*, 7(3), 237–249.
- Tada, H., Paris, P. C., & Irwin, G. R. (2000). *The stress analysis of cracks handbook*. Bury St. Edmunds, UK: Professional Engineering Publishing.
- Vinciguerra, S., Meredith, P. G., & Hazzard, J. (2004). Experimental and modeling study of fluid pressure-driven fractures in Darley Dale sandstone. *Geophysical Research Letters*, 31, L09609. <https://doi.org/10.1029/2004GL019638>
- Warpinski, N. R., Teufel, L. W., et al. (1987). Influence of geologic discontinuities on hydraulic fracture propagation (includes associated papers 17011 and 17074). *Journal of Petroleum Technology*, 39(02), 209–220.
- Wong, T. F., & Baud, P. (1999). Mechanical compaction of porous sandstone. *Oil & Gas Science and Technology*, 54(6), 715–727.
- Yew, C. H., & Liu, G. F. (1993). Fracture tip and critical stress intensity factor of a hydraulically induced fracture. *SPE Production & Facilities* (pp. 171–177).
- Zhang, Z. X. (2002). An empirical relation between mode I fracture toughness and the tensile strength of rock. *International Journal of Rock Mechanics and Mining Sciences*, 39(3), 401–406.
- Zhang, X., Wang, J. G., Gao, F., Ju, Y., & Liu, J. (2017). Impact of water and nitrogen fracturing fluids on fracturing initiation pressure and flow pattern in anisotropic shale reservoirs. *Computers and Geotechnics*, 81, 59–76. <https://doi.org/10.1016/j.compgeo.2016.07.011>
- Zhao, J. (2000). Applicability of Mohr-Coulomb and Hoek-Brown strength criteria to the dynamic strength of brittle rock. *International Journal of Rock Mechanics and Mining Sciences*, 37(7), 1115–1121. [https://doi.org/10.1016/S1365-1609\(00\)00049-6](https://doi.org/10.1016/S1365-1609(00)00049-6)
- Zia, H., Lecampion, B., & Zhang, W. (2018). Impact of the anisotropy of fracture toughness on the propagation of planar 3D hydraulic fracture. *International Journal of Fracture*, 211(1), 103–123. <https://doi.org/10.1007/s10704-018-0278-7>
- Zoback, M. D., Rummel, F., Jung, R., & Raleigh, C. B. (1977). Laboratory hydraulic fracturing experiments in intact and pre-fractured rock. *International Journal of Rock Mechanics and Mining Sciences & Geomechanics Abstracts*, 14(2), 49–58.